

Modelling the Atlantic Water along its poleward pathway into and through the Arctic Ocean
by

Chuanshuai Fu

A thesis submitted in partial fulfillment of the requirements for the degree of

Master of Science

Department of Earth and Atmospheric Sciences
University of Alberta

© Chuanshuai Fu, 2022

Abstract

The thermohaline intrusion of the warm and saline Atlantic Water (AW) into the Arctic Ocean, referred to as “Arctic Atlantification”, has significant implications and feedback on the {thermo} dynamics of the Arctic Ocean. The AW enters the Arctic Ocean through two gateways: Fram Strait and the Barents Sea Opening (BSO), and the relative strength of these two AW branches dominates the oceanic heat contribution to the Arctic Ocean. In conjunction with the measurements in key hydrographic sections, numerical ocean modelling provides us with a useful tool to characterize and corroborate the temporal and spatial variability of the AW branches. The simulations are carried out using the regional configuration the Arctic and North Hemispheric Atlantic (ANHA) of the ocean/sea-ice model NEMO running at $1/4^\circ$ and $1/12^\circ$ high resolutions. Online passive tracers from the model configurations are used to trace the pathways of the AW inflow in the Arctic Ocean.

With the AW becoming more important to the dynamics of the Arctic Ocean, this study aims to examine its variability, transformation, and impacts, as well as ultimately track how it evolves. We first evaluate the interannual and seasonal variability of the AW thermohaline structure at these two gateways, then quantify the AW volume and heat transport on the interannual and seasonal timescales. We also compare long-term transport means with the available observations. While the heat in the Fram Strait Branch Water (FSBW) dissipates in a slower process through the mixing with the ambient cold water below the sea surface, the vast majority of the heat loss of the Barents Sea Branch Water (BSBW) takes place in the Barents Sea due to the sea surface cooling. In our study, we discover two strong Cold AW anomaly events along the rim of the eastern Eurasian Basin during 2013 and 2014, overturning our understanding that the AW is always warm and saline. The dominant contributor to the Cold AW formation is the intense sea surface cooling at the Barents

Sea for two consecutive years. By releasing particles at the Barents Sea Opening and Fram Strait using an offline Lagrangian product Ariane, we find that the source of the Cold AW is primarily from the BSBW, and it also has some contributions from the FSBW. The Cold AW signals progress along the typical AW poleward pathway and eventually result in a heat content reduction in the AW layer of the eastern Arctic Basin.

Preface

Chapter 3 of this thesis has been submitted for publication as:

C. Fu, C. Pennelly, Y. Garcia-Quintana, P.G. Myers (2022): Pulses of Cold Atlantic Water in the Arctic Ocean from Ocean Model Simulation. *Journal of Geophysical Research: Oceans*. I am responsible for carrying out the experiments, analyzing data, and writing the manuscript. C. Pennelly helps with the experiment of examining the impact on the AW transformation from the surface freshwater flux. Y. Garcia-Quintana offers a tutorial using the Ariane tool for water mass study. Both also assist with providing valuable feedback on the manuscript. P.G. Myers continuously provides guidance, advice, and manuscript edits.

Acknowledgement

I would like to express my sincere gratitude to my supervisor, Paul G. Myers, for his constant support and guidance. Without him, I would not come to Canada to undertake my education and study physical oceanography in the first place. Because of him, I am living the life that I have envisioned. I can do what I enjoy for work, achieve my goals, and be on the path to pursuing my dreams.

Thank you, Kehan, for spending the late hours together in the lab (Yes, we are not early birds). I appreciate that you consider me as part of your family rather than simply a friend. I won't forget the night when we went to see the meteor storm in the Elk island national park and stayed up late until 3:30 am. Thank you, Tahya, for going through the journey together from online to in person. Thank you for your help from a linguistic aspect and your invitation to a board game night at your place. Thank you, Anthony and Lusksmi, for sharing your family with me and showing me how to raise kids with love and patience. Thank you, Seethal, Yusi, Haoran, buddies at my hometown school and home city park, and those at the university club and Edmonton table tennis club, playing table tennis with you guys adds more spice to my day-to-day life. Thank you, Jyoti, even though you have left what you called "Hellmonton", this is the city where we built up our friendship and supported each other through meal chats. Wish you all the best for your next postdoc in the UK. Thank you, Mike, my dear friend and inspiring mentor, it is you who navigate me through all the ups and downs. Thank you, Jean, I cherish the time when we cooked, talked, and played games together. Thank you, Prof. Sutherland, Dr. Mak, Prof. Guan, and Dr. Zhou, for your firm support in my PhD application and precious guidance. And thank you to all the current and previous lab

members and visiting students: Pouneh, Clark, Yarisbel, Andrew, Alain, Laura, Natasha, Liam, Kevin, Jennifer, Jan, Xiner, Ann, Germain, Nadiya, Nathen, Simon, Sreevathsa, Mukulika.

Last but not least, thank you to my family members for their unconditional love and belief in me. Thank you to all my domestic friends who are always being there when I am in need. And Adam, keep up your good work, have faith in yourself, and stay calm and carry on.

Table of Contents

List of Figures	ix
List of Tables	xiii
Abbreviations and Acronyms.....	xiv
1. Introduction	1
1.1 The North Atlantic Ocean	1
1.1.1 Atlantic Meridional Overturning Circulation	1
1.1.2 The North Atlantic Subpolar Gyre Circulation.....	3
1.1.3 The Labrador Sea and Deep Convection	4
1.2 Nordic Seas.....	6
1.3 The Arctic Ocean.....	7
1.3.1 Atmospheric and Oceanic Circulation	7
1.3.2 Sea Ice Conditions	9
1.4 Thesis Questions.....	10
2. Model description.....	16
2.1 Governing equations.....	18
2.2 Boundary conditions.....	19
2.3 Grid structure.....	25
3. Pulses of Cold Atlantic Water in the Arctic Ocean from Ocean Model Simulation	31
Abstract	32
3.1 Introduction	33

3.2	Numerical Methods	39
3.2.1	Numerical Model Description and Setup.....	39
3.2.2	Ariane and Online Passive Tracers	41
3.2.3	Transport and Content Calculations.....	43
3.2.4	Air-Sea Transformation Estimates.....	44
3.3	Results	45
3.3.1	Thermohaline Structure of the AW at Fram Strait and the BSO	45
3.3.2	Transports through the Fram Strait and BSO	50
3.3.3	AW Inflow Pathway from Online Passive Tracers.....	52
3.3.4	The Discovery and Sources of the CAW	54
3.3.5	Physical mechanisms for the CAW Formation.....	58
3.3.6	The Evolution and Fate of the CAW	60
3.4	Summary and Discussion	63
	Acknowledgments.....	66
4.	Conclusions	67
	Bibliography.....	70

List of Figures

Figure 1.1 Horizontal view of the upper (red) and lower (blue) limbs of the Atlantic Meridional Overturning Circulation (AMOC) in the Atlantic Ocean. The background colour shading depicts the main geographic features of the Atlantic Basin. LS: the Labrador Sea, NS: the Nordic Seas, DP: the Drake Passage, NASG: North Atlantic Subtropical Gyre, NASG: North Subpolar Gyre. NAC: North Atlantic Current..... 12

Figure 1.2 A schematic meridional section representing a zonally averaged picture of the Atlantic Ocean. The AMOC is denoted by the arrows below the sea surface. The general bottom bathymetry along the Atlantic Basin meridionally is represented in a grey line. Two driving mechanisms of the surface cooling in the subarctic seas and the surface wind forcing over the Southern Ocean are demonstrated. Note that in the real ocean the ratio of the meridional extent to the typical depth is about 5000 to 1. Overflow includes the Iceland-Scotland Overflow Water (ISOW) and Denmark Strait Overflow Water (DSOW); NADW: North Atlantic Deep Water; AABW: Antarctic Bottom Water..... 13

Figure 1.3 Map of the Nordic Seas with schematic surface currents: Warm and salty Atlantic Water (red) flows northward along the eastern boundary while the cold and fresh Arctic Water (blue) flows southward in the west. The cyclonic gyre circulations in the Greenland Basin, Lofoten Basin and Norwegian Basin are indicated in green. EGC: East Greenland Current; WSC: West Spitsbergen Current; NwAC: Norwegian Atlantic Current..... 14

Figure 1.4 (a) Mean pattern of sea level pressure in the Arctic, adapted from Morison et al. (2012). (b) Lateral schematic view of the water column in the Canada Basin and the atmospheric circulation above..... 15

Figure 1.5 Schematic views of the general Arctic Ocean circulation patterns under (a) low and (b) high AO index. Plans view are at the top and sections view are at the bottom (Morison et al. 2012). 15

Figure 2.1 The geographical coordinate system (λ, ϕ, z) and the curvilinear coordinate system (i, j, k). λ and ϕ are aligned with the Earth’s longitudes and latitudes respectively. i and j represent the zonal and meridional direction of the horizontal model grid respectively. z and k point to the same direction that is perpendicular to the horizontal panel (geopotential surfaces of the spherical Earth). 28

Figure 2.2 The horizontal mesh of ANHA4 and ANHA12 (colour shows the resolution in kilometres). The singular point is moved to Dease Strait from the North Pole..... 28

Figure 2.3 3D cabinet perspective (a) and 2D top-down view (b) of the variable arrangement in the NEMO mesh grid (Arakawa C-grid). The red T point in the cell center represents scalar points; The green V points, blue T points and purple W points in the center of each face indicate vector points; The gold F point in the center of each vertical edge stands for vorticity points. Three scale factors (e_1, e_2 : horizontal; e_3 : vertical) define the size of each grid cell in (a). Horizontal integer indexing has been chosen as shown in (b). The T, V, U, and F points having the same i - and j -indices are indicated by the dashed square. e_{1t}, e_{2t} is the length of the T grid cell in the horizontal plane, and so on..... 29

Figure 2.4 Vertical model grid with the traditional full step z -coordinate (left), and partial step with z -coordinate (right). Shaded cells represent the model bottom bathymetry and the dashed lines show the real sea floor..... 30

Figure 3.1 The schematic of the large-scale circulation pattern of the Atlantic Water inflow to the Arctic Ocean, with major geographic features labelled. The blue, magenta, and black lines

composed of arrows represent the FSBW, BSBW, and AWBC respectively. The locations of the Arctic gateway straits (F1 and B1) and sections along the poleward pathway (B2, S1, S2, S3, S4 and S6) are indicated. Contour lines are -200 m, -500 m, -1000 m and then -2000 m. FS: Fram Strait, BSO: Barents Sea Opening, CAA: Canadian Arctic Archipelago..... 38

Figure 3.2 Annual mean temperature T (a & d, unit: °C), salinity S (b & e), and normal to cross-section velocity v (c & f, unit: cm/s) at Fram Strait (Upper panel) and the BSO (Lower panel) in 2013. The velocity is positive towards the Arctic Ocean. The isopycnal lines are contoured onto the temperature and salinity fields in Fram Strait. The x-axis shows the distance (Fram Strait: from west to east; BSO: from north to south) in kilometres the y-axis shows the ocean depth in metres..... 47

Figure 3.3 Top row: the interannual variability of volume (blue) and heat transport (red) for the Atlantic Water at Fram Strait (a) and the BSO (b) over 2011-2019 with standard error estimates included (standard deviation over the square root of the number of the data samples). Bottom row: Fram Strait (c) and the BSO (d), but for the seasonal variability. The heat transport is referenced to 0 °C. Positive values mean towards the Arctic Ocean, i.e. transports are positive northwards across Fram Strait and eastwards across the BSO. 51

Figure 3.4 A snapshot of the vertically integrated AW tracer concentration on June 4, 2019 (a) particles are released from a combination of Fram Strait and the BSO; (b) from Fram Strait solely; (c) from the BSO solely. 53

Figure 3.5 (a) Monthly AW volume transport at S3 from 2011-2019; (b) Monthly CAW volume transport at Barent2 (B2), Section1 (S1), Section2 (S2), Section3 (S3), Section4 (S4) and Section6 (S6) from 2011-2019; The locations of each section are shown in Figure 3.1..... 56

Figure 3.6 (a) Distribution of particles in the BSO seeded in July 2012. (b) Distribution of all the particles after a two-year forward simulation scheme, that is, a snapshot in July 2014. (c) Only exhibit the particles with a temperature below 0 °C at the AW layer (between 400-1200 m deep) from (b). 58

Figure 3.7 (a) The CAW cross-isopycnal volume fluxes (Sv) changing with the surface density anomaly (kg/m^3) in 2013. The red and blue lines exhibit the transformation rate due to heat and freshwater fluxes, respectively. The black line is the sum of both. (b) the spatial pattern of the transformation rate at $\sigma^* = 28.1 kg/m^3$ and $\Delta\sigma = 0.05 kg/m^3$. (c) the interannual variability of the transformation rate for the CAW from 2011 to 2019. 59

Figure 3.8 (a) Distribution of particles in B2 seeded in July 2013. (b) The locations of the particles after evolving for 15 days, 30 days, and 50 days. (c) The locations of the particles at the end of the simulation, on December 31, 2019. 62

Figure 3.9 (a) The simulated region in the Arctic Basin, indicated in blue quasi-parallelogram. (b) the heat content and (c) the freshwater content integrated from the whole water column from 2011 to 2019. 63

List of Tables

Table 3.1 NEMO Experiments using the ANHA configuration.	41
Table 3.2 Long-term means of the AW temperature, oceanic volume and heat transport through Fram Strait and the BSO from ANHA4, ANHA12 and available observations. ANHA4: averaged over 2011-2016; ANHA12: averaged over 2011-2019; a: Mean over 1997-2010 from Beszczynska-Möller et al. (2012); b: Mean over 1997-2006 from Schauer et al. (2008); c: Mean over 1997-2007 from Smedsrud et al. (2010).....	48
Table 3.3 The duration of the apparent CAW signals at some sections in 2013 and 2014. The CAW pulses are apparent when the volume transport is larger than 3 Sv at S3, and it is larger than 2 Sv for the other sections.	56

Abbreviations and Acronyms

AW	Atlantic Water
PW	Pacific Water
AMOC	Atlantic Meridional Overturning Circulation
AABW	Antarctic Bottom Water
ISOW	Iceland-Scotland Overflow Water
DSOW	Denmark Strait Overflow Water
LSW	Labrador Sea Water
NADW	North Atlantic Deep Water
NASG	North Atlantic Subpolar Gyre
NAC	North Atlantic Current
WGC	West Greenland Current
BIC	Baffin Island Current
NAO	North Atlantic Oscillation
SLP	Sea Level Pressure
IRs	Irminger Rings
BCEs	boundary current eddies
CEs	convective eddies
BSO	Barents Sea Opening
FS	Fram Strait

NwAC	Norwegian Atlantic Current
SSH	Sea Surface Height
SLP	Sea Level Pressure
AO	Arctic Oscillation
CAA	Canadian Arctic Archipelago
NEMO	Nucleus for European Modelling of the Ocean
OPA	Océan PARallélisé
LIM	Louvain-la-neuve Ice Model
TOP	Tracer in the Ocean Paradigm
ANHA	Arctic and Northern Hemisphere Atlantic
CAW	Cold Atlantic Water
FSBW	Fram Strait Branch Water
BSBW	Barents Sea Branch Water
WSC	West Spitsbergen Current
ArW	Arctic Water
EGC	East Greenland Current
AWBC	Atlantic Water Boundary Current
GLORYS2v3	GLobal Ocean ReanalYsis and Simulations 2 version 3
CGRF	Canadian Meteorological Centre's (CMC) Global Deterministic Prediction System (GDPS) ReForecasts
HYPE	HYdrological Predictions for the Environment

1. Introduction

This chapter reviews the dynamics of the North Atlantic Ocean, the Nordic Seas, and the Arctic Ocean. It also lists the research questions we were trying to address. Due to the fact that the sea surface elevation of the Pacific Ocean is higher than that of the Arctic Ocean, Pacific Water (PW) is exported to the Arctic Ocean. In the meanwhile, the Atlantic Water (AW) also flows into the Arctic Ocean, and it is warmer and saltier, with an inflow transport 10 times larger than the PW inflow. Therefore, the interaction between the Arctic Ocean and the North Atlantic Ocean is much more intimate. This process is principally achieved via the Nordic Seas and the Arctic gateways.

1.1 The North Atlantic Ocean

1.1.1 Atlantic Meridional Overturning Circulation

As the second largest of the five major oceans, the Atlantic Ocean is the saltiest on average. It is composed of the North Atlantic Ocean and the South Atlantic Ocean, separated by the Equatorial Counter Current at around 8°N . In the Atlantic Ocean, the Atlantic Meridional Overturning Circulation (AMOC), often delineated as a conveyor belt driven by both atmospheric and thermohaline circulations, plays a leading role in transporting and distributing a great amount of heat and salt from the tropics to the polar regions (Frierson et al., 2013), and sinking nutrients and gases (including oxygen and human-induced carbon) into the deeper ocean (Rhein et al., 2017). It is characterized by the northward flows of warm saline water in approximately the upper 1000 m (the upper AMOC limb) and returning flows of cold fresh denser water in the intermediate and deep layers (the lower AMOC limb) (Figure 1.1 and Figure 1.2). The upper/lower limbs of AMOC are defined as the transport between the sea surface/bottom and the maximum of the overturning

stream function, representing the total northward/southward transport of the zonally integrated meridional flow. Cross-basin observations are presently occurring at two locations. The zonal integral is calculated in depth space in the subtropical Atlantic Ocean (e.g. The RAPID Array at 26.5°N, see Mccarthy et al. (2012)), whereas density coordinates are used by the group making measurements in the subpolar Atlantic Ocean (e.g. The OSNAP section, see Lozier et al. 2019). The isobath of 1100 m and the isopycnal of 27.66 kg m^{-3} separate the upper and lower limbs of the AMOC, respectively. The application of the different coordinates is to accommodate the dominance of diapycnal mixing and strongly sloped isopycnals in the subpolar North Atlantic. The energy redistribution from the AMOC help ease the latitudinal energy gradients owing to equator-concentrated solar heating of the Earth. Lagrangian particle trajectories reveal the significance of mesoscale eddies in the AMOC transport mechanism in some regions and the lack of meridional connectivity due to the recirculation gyres in both limbs of the AMOC (Bower et al., 2019) (Figure 1.1). The AMOC depicts the vigorous oceanic dynamics in the Atlantic Ocean and is a vital component of the global climate system. The AMOC is projected to weaken in the coming century due to a reduction in deep convection in the North Atlantic (Lozier et al., 2019), induced by anthropogenic climate change (Mccarthy et al. 2020). The evolution of the AMOC may have profound climate impacts and reflects the future Atlantic Ocean circulation.

The Antarctic Bottom Water (AABW) originates on the continental shelves of Antarctica, where brine rejection during sea ice formation in coastal polynyas and below the ice shelf densifies the seawater (Matsumoto, 2017). AABW flows northward along the bottom boundary layer and gradually rises into the lower limb of the AMOC, forming a deeper overturning cell (Figure 1.2). The AMOC is principally driven by both thermohaline mixing and atmospheric forcing processes.

Surface cooling leads to the deep water formation in the northern North Atlantic, contributing to the transformation from the upper limb to the lower limb. In the Labrador Sea, deep convection events occur intermittently due to the wintertime cooling, in which the mixed water layer could extend down as far as 2000 m or so (Yashayaev & Loder, 2016). The deep water originating in the Nordic Seas flows southward over the Greenland-Iceland-Scotland Ridge, becoming the Iceland-Scotland Overflow Water (ISOW) and Denmark Strait Overflow Water (DSOW). In conjunction with the Labrador Sea Water (LSW), they comprise the North Atlantic Deep Water (NADW), establishing the lower limb of the AMOC (Haine et al., 2008). Another driving mechanism is the surface wind forcing over the Southern Ocean (Kuhlbrodt et al., 2007). The strong westerly wind along the latitude band of the Drake Passage causes the divergence of the Ekman transport and Ekman upwelling that pumps the waters up to the surface (Buckley & Marshall, 2016). These two mechanisms function as motors that provide the energy to maintain the steady state of the AMOC.

1.1.2 The North Atlantic Subpolar Gyre Circulation

The ocean surface circulation in the North Atlantic Ocean is manifested as the permanent, large-scale North Atlantic Subtropical Gyre and the North Atlantic Subpolar Gyre (NASG). The latter is characterized by cyclonic boundary currents and interior recirculation. The NASG consists of several branches of the North Atlantic Current (NAC) at its equatorward side between 45 °N and 55 °N, flowing eastward as an extension of the Gulf Stream (Holliday et al., 2018). Part of the NAC recirculates and forms the Irminger Current when reaching the west Irminger Sea as the boundary currents of the NASG. Another boundary current is East Greenland Current, it has a warm and salty component formed by the recirculating Irminger Current and a cold and fresh component that flows south through the Denmark Strait. The East Greenland Current loops around Cape Farewell along the undersea topography and becomes the West Greenland Current (WGC).

It turns cyclonically southward around Northwest Labrador Sea and is joined by the Baffin Island Current (BIC) and by outflow through Hudson Strait. The combined flow forms the Labrador Current, which continues southward and separates around the Grand Banks of Newfoundland, with the majority of the current flowing eastwards to complete the NASG (Fratantoni & Pickart, 2007; Holliday et al., 2018; Myers et al., 2009). Since the NASG is adjacent to Greenland, the surplus meltwater of the Greenland Ice Sheet impacts the freshwater transport in the WGC and thus potentially affects the NASG (Dukhovskoy et al., 2015; Myers et al., 2009). The dynamic of the NASG circulation could regulate the deep water formation rate and thus influence the AMOC.

The NASG circulation is modulated by the synoptic atmospheric circulation associated with the North Atlantic Oscillation (NAO). The NAO index symbolizes the strength of the Icelandic Low (the Subpolar Low) and the Azores High (the Subtropical High) and describes the Sea Level Pressure (SLP) variability, establishing the wind stress curl pattern in the North Atlantic Ocean (Chafik et al., 2015). The prevailing westerly wind across the North Atlantic is an indispensable driving force to the NAC (Isachsen et al., 2014). A positive NAO index indicates that these two recurring pressure patterns are intense, thereby a drastic pressure gradient, creating a strong westerly wind. In this case, a more powerful NAC potentially transports a larger amount of the warm and saline AW towards higher latitudes. On the contrary, the westerly wind is weak when the NAO is in a negative phase.

1.1.3 The Labrador Sea and Deep Convection

The Labrador Sea, a semi-enclosed basin in the northwestern part of the North Atlantic, is a region known to have a direct impact on the processes that control climate change, where deep convection occurs. Deep convection occurs when there is a weakly stratified ocean water column beneath the

surface mixed layer that undergoes a great amount of heat loss. The heat loss is attributed to the winter-time atmospheric conditions and so its variability is linked to the variation in the NAO. The direct effect of heat loss is responsible for reducing the ocean buoyancy, resulting in the preconditioning of the deep convection. Therefore, the cold and dense surface water sinks into the subsurface while a net flux of heat and salt is ventilated up to the surface layers. This is the deep convection. The convective process leads to the water mixing and thus the formation of the homogenous Labrador Sea Water (LSW). The predicted site of the deepest mixed layer in the southwestern quadrant of the Labrador Sea is the overlapping part between the regions of maximum buoyancy loss and weak stratification (Marshall et al., 1998). The intermittent recurrence of strong convection is predominantly governed by the intensified winter atmospheric cooling anomaly. It dominates the decadal-scale variability of mid-depth LSW properties (Yashayaev & Loder, 2016).

In addition to the vertical physical mixing, the deep convection also plays a crucial role in the biological cycle that has significant implications with respect to climate change. Rhein et al. (2017) found that the variability in the LSW formation regulates the spatial distribution and storage of oxygen and anthropogenic carbon uptake in the Labrador Sea. During the years with strong deep convection, more oxygen and anthropogenic carbon could be taken into the deeper ocean, oxygenating the interior of the ocean and slowing the accumulation of anthropogenic carbon in the atmosphere. With the cessation of the deep convection in the late winter, the lateral interior-boundary current exchange takes a leading position, contributing to the restratification in the interior region and the export of the LSW. The lateral exchange occurs at a rapid rate in the first few months following convection due to the large difference in the mean horizontal interior-boundary current density, then persists at a slower rate throughout the entire year (Straneo, 2006).

While the lateral exchange flattens the density gradients, three kinds of eddies are likely to be generated to facilitate the process: The Irminger Rings (IRs) are produced by the barotropic instability of the boundary current off Cape Desolation. They are the largest type with the highest eddy kinetic energy and densely populate the basin north of 58°N; The boundary current eddies (BCEs) are spawned by weakly energetic boundary current instabilities and found offshore of the West Greenland and Labrador coasts; The convective eddies (CEs) appear due to the baroclinic instability of steep isopycnal slopes owing to the late winter deep convection (Chanut et al., 2008). These three distinct eddies orchestrate the convergence of heat and salt and transfer the properties of the boundary current to the central Labrador Sea, hence helping to reset a weak density stratification for subsequent convection.

1.2 Nordic Seas

The Nordic Seas connect to the Arctic Ocean through two Arctic gateways: namely Fram Strait and the Barents Sea Opening (BSO) and also to the North Atlantic Ocean through the Denmark Strait and the Greenland-Scotland Ridge (Figure 1.3). Owing to their location, the Nordic Seas become an important site for the communication between the Arctic Ocean and the North Atlantic Ocean, in particular the penetration of their respective water mass properties. The Nordic Seas encompass the Greenland Sea, the Iceland Sea and the Norwegian Sea. Part of the NAC flows into the Norwegian Sea through the Greenland-Scotland Ridge and forms the Norwegian Atlantic Current (NwAC), continuously feeding the warm and saline AW into the subarctic seas. The AW inflow is crucial to deep water formation in the Nordic Seas and heat and salt fluxes are expected to further increase in the context of global warming and the intensified water cycle. Due to the bathymetry setting in the Nordic Seas, the flows are topographically steered and generate cyclonic gyres in the Greenland basin and the other two basins of the Norwegian Sea (Raj et al. 2019).

Sea ice is formed in the northwestern part of the Nordic Seas during the winter months, whereas the majority of the region remains ice-free in the summer. The heat transport anomalies occurring downstream of the NwAC become a good predictor of the variance of the Nordic Seas ice cover (Schlichtholz, 2011). The cooling of the NwAC along its transit across the Nordic Seas could be ascribed to the lateral eddy fluxes, the heat loss to the atmosphere, and the heat absorbed by the sea ice melt (Isachsen et al., 2012). The heat content in the Nordic Seas varies over seasonal to decadal timescales, which is found to be closely associated with both advective processes and air-sea interactions. The advective processes include the advective heat transport through both the entrances and exits. The atmosphere-ocean heat flux depends on the winter atmospheric condition that is linked to the variability of the atmospheric circulation characterized by the NAO (Chafik et al., 2015). The Nordic Seas have become warmer and saltier in the recent two decades compared with the average ocean state in the past. The warming is governed by the changes in both reduced sea surface heat loss and increased advective heat flux, and the salinification is mainly a result of the diminishing sea ice flux from the Arctic Ocean (Tesdal & Haine, 2020). The incremented salinity further decreases the Sea Surface Height (SSH) and strengthens the cyclonic gyre circulation in the Nordic Seas (Wang et al., 2020).

1.3 The Arctic Ocean

1.3.1 Atmospheric and Oceanic Circulation

The Arctic Ocean is not only the smallest and shallowest but also the coldest and freshest (top 200 m) of the five major oceans on Earth. The oceanic circulation of the Arctic Ocean is driven by the sea level pressure regulated by the atmospheric systems, the dynamic height gradient induced by the seawater density change, and the topographic setting. It is also modulated by the melting and

growth of sea ice. The Arctic Ocean is a typical example of a coupled atmosphere-ice-ocean dynamic system. It has experienced drastic changes in recent decades, especially with the additional anthropogenic forcing such as greenhouse gas warming. The Arctic is warming faster than the rest part of the globe, so-called “Arctic Amplification”. Therefore, understanding the manifestations, mechanisms, and ramifications of such dynamic change is a top priority.

The mean Sea Level Pressure (SLP) in the Arctic is characterized by two leading atmospheric pressure systems: the anticyclonic Beaufort High centred over the Canadian Basin and the cyclonic Icelandic Low situated near Iceland in the North Atlantic Ocean. These two waxing and waning wind patterns shift from one to another on a timescale of 5-7 years, dominating the synoptic surface oceanic circulation of the Arctic Ocean: the Beaufort Gyre and the Transpolar Drift Stream (Timmermans and Marshall 2020). The anticyclonic Beaufort Gyre is governed by the Beaufort High centred over the Canadian Basin. It forces the convergence of Ekman transport in the upper ocean, and the subsequent Ekman pumping leads to the higher SSH and the deepening of isohaline surfaces in the centre (Figure 1.4). This is because the fresher water on the surface gets pulled down into the interior at depth. The interannual freshwater accumulation is controlled by the geostrophic ocean circulation and the Ekman transport convergence mechanism (Proshutinsky et al., 2019). The pathway and strength of the Transpolar Drift Stream are linked to the central positions and intensity of the Beaufort High and Icelandic Low, carrying the sea ice and water across the Arctic Ocean towards Fram Strait (Timmermans & Marshall, 2020).

The Arctic Oscillation (AO), the spatial pattern of the first Empirical Orthogonal Function (EOF) of Northern Hemisphere SLP, is used to describe Arctic atmospheric variability. It manifests itself

as a trough of low pressure extending from the Nordic Seas to the Eurasian Basin and then forms the westerly “polar vortex” over the Arctic. The AO index, the amplitude of the leading EOF, could determine the strength of the low pressure anomaly and the wind pattern. It has a strong interannual variability and has been trending to be in a positive regime for the last 30 years. During the years with a moderately high AO index, combined with the mean SLP pattern, it can produce an anticyclonic-cyclonic dipole oceanic circulation in the Arctic Ocean (Figure 1.5). The anticyclonic Beaufort Gyre is weaker and restricted to the Canada Basin, whilst the Transpolar Drift Stream flows nearly directly from the Bering Strait to the Fram Strait. The cyclonic circulation in the Eurasian basin transports the river runoff from the Eurasian continental shelf eastward and injects it as a geostrophic current into the Beaufort Gyre, enhancing the freshwater content accumulation in the Canada Basin. In contrast, in the low AO anticyclonic mode, the Beaufort Gyre strengthens and expands over most of the basin, and the orientation of the Transpolar Drift Stream shifts towards the Lomonosov Ridge with the runoff transport following its path (Morison et al., 2012).

1.3.2 Sea Ice Conditions

The sea ice cover and thickness are sensitive to global warming. Therefore, the variability becomes one of the most visible representations to diagnose the thermodynamic impact on the Arctic Ocean. The sea ice cover exhibits a strong seasonal variability with the maximum in March and the minimum in September. The findings from the observations and models unanimously have demonstrated that the Arctic Sea minimum ice cover in September has been decreasing substantially since the late 1970s and the ongoing downward trend is accelerating (Stroeve et al. 2007; Cavalieri and Parkinson 2012). The studies also show that the observed and modelled March trends are much smaller and not significant, this implies that the thermodynamic impact is reflected in the sea ice thickness rather than the extent during the winter months. Comiso (2012) confirms

that the multiyear sea ice has been becoming thinner and younger with a periodic 8 to 9-year cycle by analyzing the satellite observations from 1979 to 2011. The year 2012 marked a record minimum sea ice extent since 1979. The decreased sea ice volume change is strongly correlated with the increased Arctic Ocean surface temperature induced by both natural variability and anthropogenic forcing; the latter is playing a dominant role.

During the formation of sea ice, the cold and salty brine sinks because of its higher density. This brine contributes to the formation of the Arctic Bottom Water and the establishment of stratification in the vertical structure. The capping sea ice suppresses the wind-driven stirring and mixing. However, with the status quo of having more melting sea ice, the atmospheric circulation would have more effect on the oceanic circulation and stratification. The melt of sea ice also triggers the positive feedback of the ice-albedo mechanism. The decreased albedo from sea ice to liquid water during the melting process enables more shortwave radiation absorption and hence enhances the melting (Stroeve et al., 2007). The mobile sea ice drifts with both the oceanic circulation and wind pattern and can pile up in some regions. Similarly, it responds to the atmospheric circulation changes associated with the AO index. (Comiso, 2012; Howell et al., 2015).

1.4 Thesis Questions

With the streams of the AW inflow becoming more important to the dynamics of the Arctic Ocean, my aim is to examine its variability, transformations, and impacts along its poleward pathway, as well as ultimately track how it evolves after it enters the Arctic Ocean. With the application of an ocean model, we study its variability by measuring its variations in temperature, salinity, momentum and other physical properties. Therefore, we can calculate its volume and heat transport at some key sites and the heat content in the Arctic Basin to detect the influence of the AW.

Additionally, we can represent and parametrize the crucial processes that could result in the transformation of the AW, such as the surface heat and freshwater fluxes. By doing analysis with the model results, verified with the observations, we are able to probe the mechanisms behind driving the manifested trend and variability. The following questions will be answered to achieve the goals of this thesis:

- What are the characteristics, mean state and variability of the AW hydrographic properties at both Fram Strait and the BSO? How do the results compare with the observations and estimates from various other model studies?
- What are the pathways and circulation patterns of the AW in the Arctic Ocean? How could the thermohaline structure and strength of the AW boundary current be altered propagating along the continental slope of the Eurasian Basin and travelling far enough to enter the Canadian Basin? What processes are contributing to the variability and how does it connect to the variability upstream at the entry gateways? Does the AW also reach the shelf north of the Canadian Arctic Archipelago (CAA) and/or penetrate the northern CAA. If so, by what pathways, and how does it evolve with time?

This thesis is divided into five chapters. It begins with a literature review in chapter 1. Chapter 2 gives a brief overview of the ocean model and provides a basic background for the experiments. Chapter 3 is drafted to answer the research questions and present the key findings. Chapter 4 summarizes this thesis and comes up with future research plans. Bibliography lists all the references.

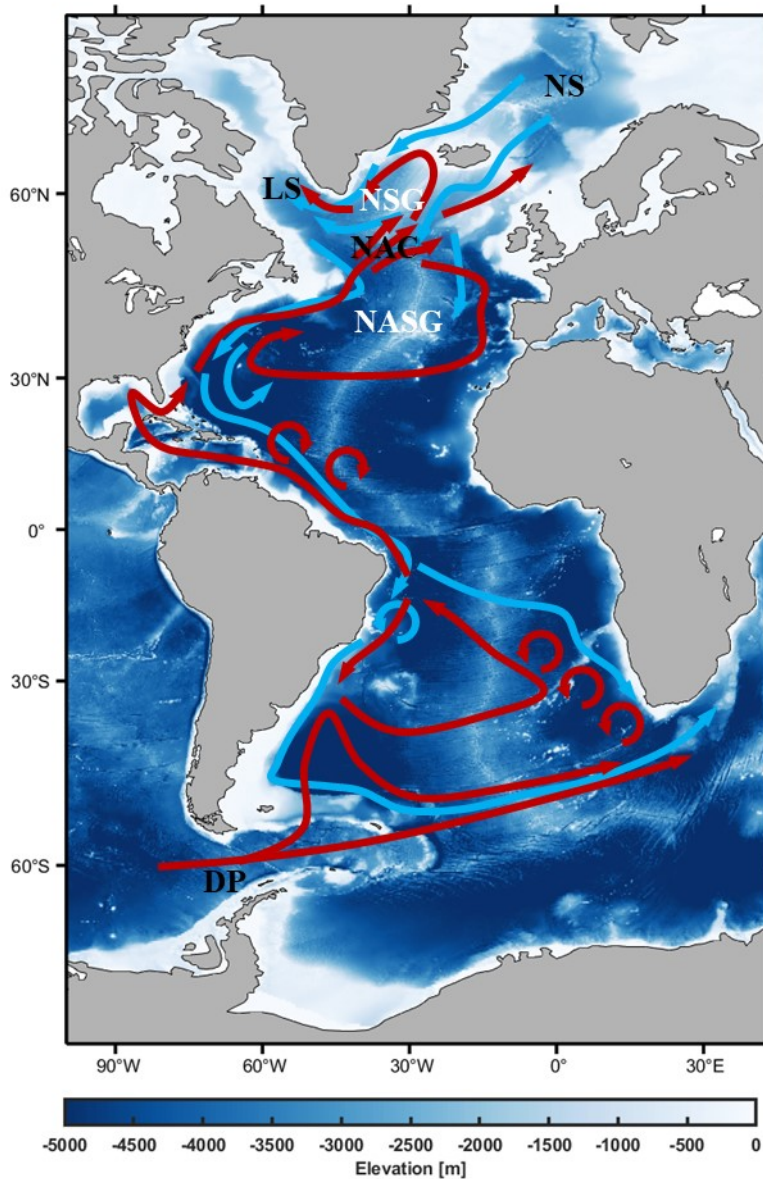


Figure 1.1 Horizontal view of the upper (red) and lower (blue) limbs of the Atlantic Meridional Overturning Circulation (AMOC) in the Atlantic Ocean. The background colour shading depicts the main geographic features of the Atlantic Basin. LS: the Labrador Sea, NS: the Nordic Seas, DP: the Drake Passage, NASG: North Atlantic Subtropical Gyre, NASG: North Subpolar Gyre. NAC: North Atlantic Current.

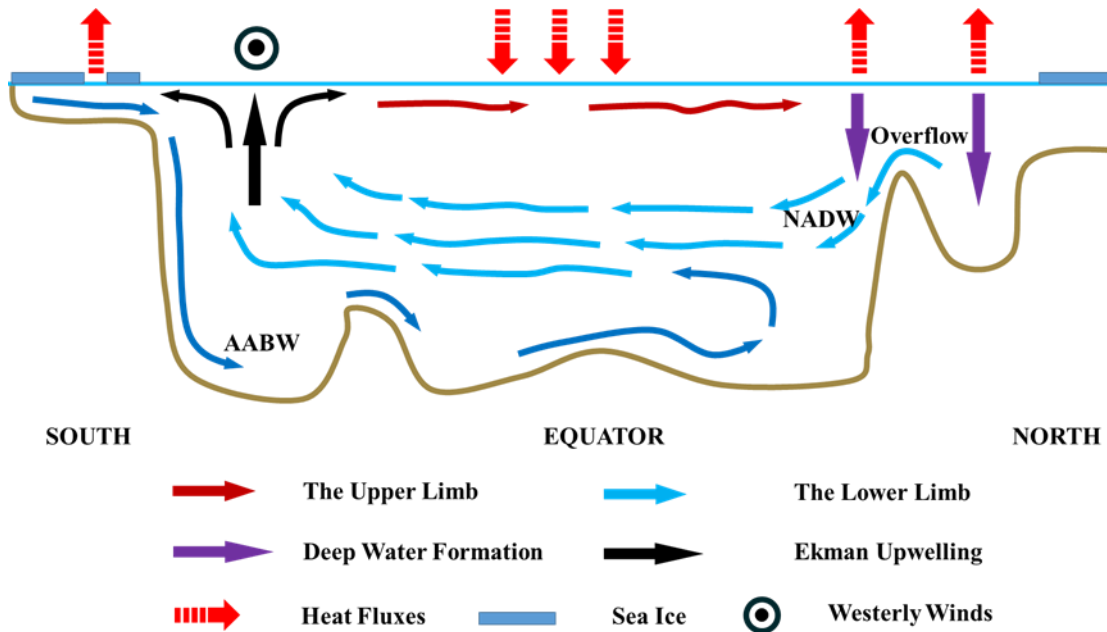


Figure 1.2 A schematic meridional section representing a zonally averaged picture of the Atlantic Ocean. The AMOC is denoted by the arrows below the sea surface. The general bottom bathymetry along the Atlantic Basin meridionally is represented in a grey line. Two driving mechanisms of the surface cooling in the subarctic seas and the surface wind forcing over the Southern Ocean are demonstrated. Note that in the real ocean the ratio of the meridional extent to the typical depth is about 5000 to 1. Overflow includes the Iceland-Scotland Overflow Water (ISOW) and Denmark Strait Overflow Water (DSOW); NADW: North Atlantic Deep Water; AABW: Antarctic Bottom Water.

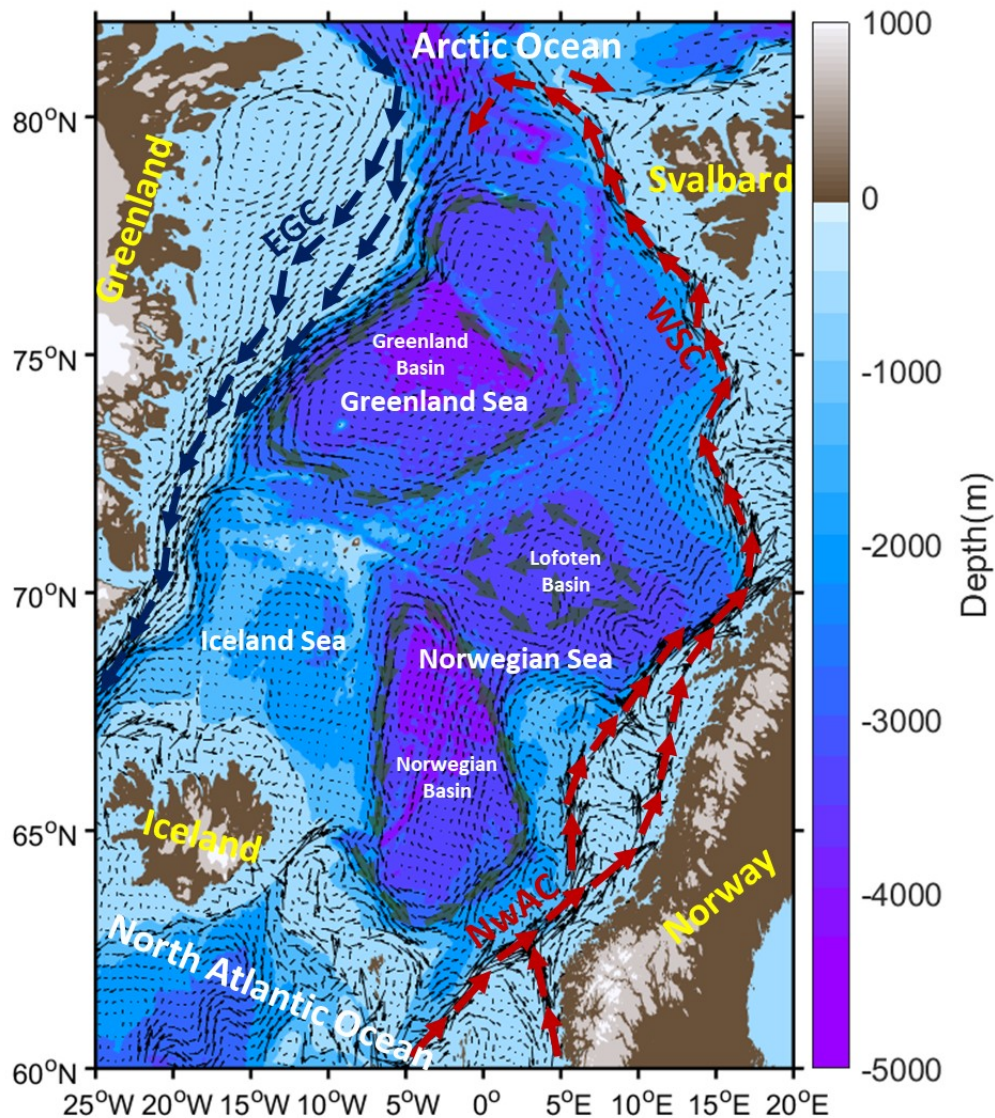


Figure 1.3 Map of the Nordic Seas with schematic surface currents: Warm and salty Atlantic Water (red) flows northward along the eastern boundary while the cold and fresh Arctic Water (blue) flows southward in the west. The cyclonic gyre circulations in the Greenland Basin, Lofoten Basin and Norwegian Basin are indicated in green. EGC: East Greenland Current; WSC: West Spitsbergen Current; NwAC: Norwegian Atlantic Current.

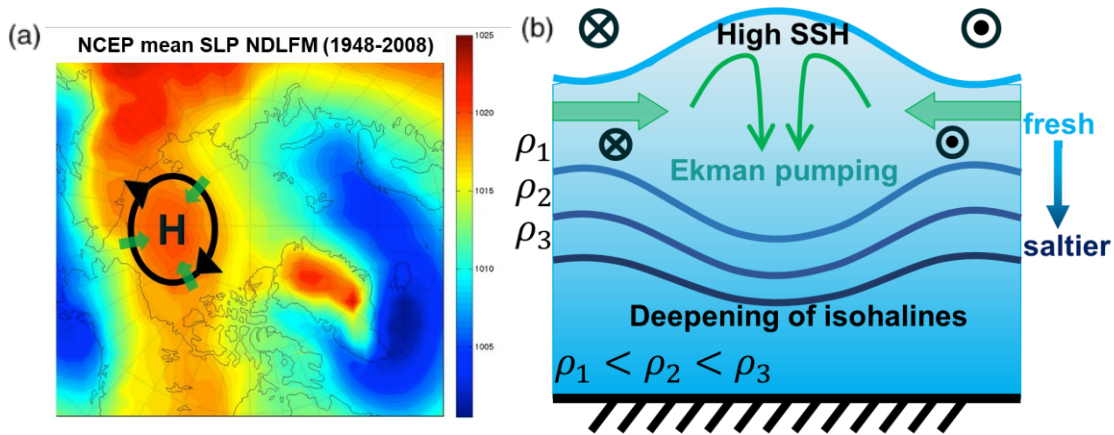


Figure 1.4 (a) Mean pattern of sea level pressure in the Arctic, adapted from Morison et al. (2012). (b) Lateral schematic view of the water column in the Canada Basin and the atmospheric circulation above.

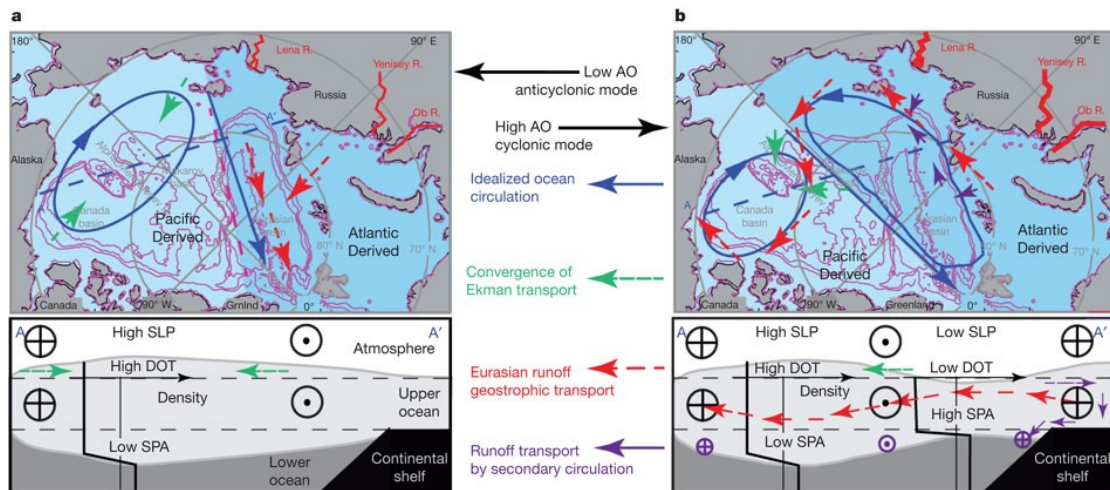


Figure 1.5 Schematic views of the general Arctic Ocean circulation patterns under (a) low and (b) high AO index. The plans view is at the top and the section view is at the bottom (Morison et al. 2012).

2. Model Description

In conjunction with the fluid dynamics theory and the hydrographic observations, numerical ocean modelling provides us with a useful tool to characterize the temporal and spatial variability and thus better predict ocean evolution in the future. An ocean model is a mathematical and computational description of the general state of the ocean, simulating the seawater properties and representing the thermodynamic and mechanical forcings that affect them. It is a system of postulates, data, and inferences that involves solving a series of coupled partial differential equations in discretized time and space. Ocean models are currently in a phase of rapid development and expanding utilization. As a result of the advanced improvement in computing power, the ocean model is now equipped with a much higher spatial resolution to resolve the mesoscale ocean dynamics and the circulation features.

The Nucleus for European Modelling of the Ocean (NEMO; available at <https://www.nemo-ocean.eu>) is a state-of-art numerical modelling framework that is used to study the ocean and its other components of the Earth's climate system over a wide range of time and space scales (Madec, 2016). It has three major components that can be coupled together, including Océan PARallélisé (OPA) engine for ocean dynamics and thermodynamics, Louvain-la-neuve Ice Model (LIM) module for sea-ice dynamics and thermodynamics, and Tracer in the Ocean Paradigm (TOP) for the online passive tracers. The analysis that has been done in this thesis is based on these components.

The ocean component of NEMO is governed by a set of fluid dynamic primitive equations and a nonlinear equation of state that represents the thermodynamic. Some useful approximations and hypotheses are applied to simplify ocean modelling and reduce the computing cost.

1. **Spherical Earth approximation:** The Earth is a planet that has bulges (more mass) and dimples (less mass) on the surface. In the ocean model, the Earth is assumed to be a body of uniform mass in spherical shape so that the resulting gravity is always perpendicular to the geoid.
2. **Thin Shell approximation:** The ocean depth is ~ 4 km on average and ~ 11 km maximum which is much smaller than the Earth's radius of ~ 6400 km, thus the ocean depth is neglected compared to the Earth's radius. The distance from any location within the ocean to the center of the Earth is equal to the Earth's radius.
3. **Turbulent closure hypothesis:** Ocean currents can be decomposed to the time-mean flow and the turbulent flow. The turbulent flow that represents the effect of sub-grid scale processes on the large-scale, is parameterized in terms of the large-scale features.
4. **Boussinesq approximation:** Over most of the ocean, even though the density varies, the change in density is no more than 2% from a reference value of $\rho_o = 1026 \text{ kg/m}^3$. Therefore, density variations are negligible except in their contribution to the buoyancy force.
5. **Hydrostatic hypothesis:** The vertical momentum equation is approximated to be in hydrostatic balance, where the vertical pressure gradient is balanced by the buoyancy force. The convective processes from the vertical momentum equation are parameterized in the ocean model.
6. **Incompressibility hypothesis:** The fluid is considered to be incompressible, then the density of the fluid does not change during its motion,

$$\frac{D\rho}{Dt} = 0 \quad (2.1)$$

According to the continuity equation that is corresponding to the mass conservation law,

$$\frac{\partial \rho}{\partial t} + \nabla \cdot (\rho \vec{u}_3) = \frac{D\rho}{Dt} + \rho \nabla \cdot \vec{u}_3 = 0 \quad (2.2)$$

results in that the divergence of the velocity field is zero

$$\rho \nabla \cdot \vec{u}_3 = 0 \quad (2.3)$$

$$\nabla \cdot \vec{u}_3 = 0 \quad (2.4)$$

2.1 Governing equations

With the mathematical assumptions, six primitive equations describe the state of the ocean. They are the horizontal momentum equation (2.5), hydrostatic balance (2.6), the incompressibility equation (2.7), the conservation equation for heat (2.8), and the conservation equation for salt (2.9), and the equation of state (2.10).

$$\rho_o \left(\frac{\partial \vec{u}}{\partial t} + \vec{u} \cdot \nabla \vec{u} + 2\vec{\Omega} \times \vec{u} \right) = -\nabla p + \vec{F}_u + \vec{D}_u \quad (2.5)$$

$$\frac{\partial p}{\partial z} = -\rho g \quad (2.6)$$

$$\nabla \cdot \vec{u}_3 = 0 \quad (2.7)$$

$$\left(\frac{\partial T}{\partial t} + \vec{u}_3 \cdot \nabla T \right) = F_T + D_T \quad (2.8)$$

$$\left(\frac{\partial S}{\partial t} + \vec{u}_3 \cdot \nabla S \right) = F_S + D_S \quad (2.9)$$

$$\rho = \rho(T, S, p) \quad (2.10)$$

Where

$\vec{u} = (u, v)$ is the horizontal velocity vector

$\vec{u}_3 = (u, v, w)$ is the three-dimensional velocity vector, also note that u, v and w denote the zonal (east-west), meridional (north-south) and vertical (up-down) velocities respectively;

$\nabla = \frac{\partial}{\partial x} \vec{e}_x + \frac{\partial}{\partial y} \vec{e}_y + \frac{\partial}{\partial z} \vec{e}_z$ is the gradient derivative vector operator;

$\vec{u} \cdot \nabla \vec{u}$ is the nonlinear inertia term that represents the self-advection of a fluid parcel,

$-\nabla p$ is the negative pressure gradient that refers to the fluid parcel moving from high pressure to low pressure;

$\vec{\Omega} = \Omega \vec{e} = \frac{2\pi}{T} \vec{e}$ is the angular frequency pointing to the North Pole (On Earth, $\Omega \approx 7.29 \times 10^{-5} s^{-1}$), and $2\vec{\Omega} \times \vec{u}$ represents the Coriolis effect.

Surface forcing terms are \vec{F}_u, F_T and F_S , and parameterizations of diffusion for momentum, temperature and salinity are \vec{D}_u, D_T and D_S , respectively.

The advection term for temperature and salinity are $\vec{u}_3 \cdot \nabla T$ and $\vec{u}_3 \cdot \nabla S$ respectively.

The reference density is ρ_o , the potential density is ρ , the potential temperature is T , the practical salinity is S , the pressure is p and the magnitude of gravitational acceleration is g .

2.2 Boundary conditions

The boundary conditions of NEMO are constrained by the contact between the ocean and the bottom bathymetry at the base and the interfaces of the air-sea or ice-sea at the top. The sea floor depth is set as $z = -H(i, j)$ and the Sea Surface Height (SSH: the instantaneous sea level above or below the ellipsoid of $z = 0$) is defined as $z = \eta(i, j, k, t)$. The ocean interacts with the land,

atmosphere, and sea ice by exchanging the heat, freshwater, salt, and momentum fluxes. However, some of the fluxes are small and can be neglected in the ocean model.

Ocean-land boundary: Two types of the ocean-land interface exist in the ocean model. One is the freshwater flux through river runoff between the ocean and continental margins. The freshwater input (salinity=0) from the river discharge and the glacial melt from Greenland has greatly reduced the sea surface salinity near the estuaries and fjords. To simulate freshwater flux, the global monthly river discharge data ($1^\circ \times 1^\circ$) from Dai et al. (2009) and the interannual monthly Greenland meltwater data ($5 \text{ km} \times 5 \text{ km}$) provided by Bamber et al. (2012) are remapped onto the model grid. The river runoff dataset is based on Global River Flow and Continental Discharge Dataset (Dai & Trenberth, 2002). It ends in 2007 while the Greenland meltwater dataset goes up to 2010. After that, the source data from the last year are repeated for the rest of the years until the end of the simulation. An updated runoff dataset from the HYdrological Predictions for the Environment (HYPE) is also used in some experiments to cover both major rivers and local runoff and simulate a more realistic freshwater flux (Stadnyk et al., 2021).

The other type of the ocean-land boundary condition is the heat and salt fluxes via the ocean-solid Earth interface, but they are too negligible in the ocean model and thus set to be zero. In terms of momentum, a free-slip scheme is applied, which means the velocity normal to the sea floor and coastline is zero while the velocity tangent to the solid boundaries remains. The kinematic boundary condition is expressed as:

$$w = -\vec{u} \cdot \nabla_z H \quad (2.11)$$

where w is the vertical velocity, $\nabla_z = \frac{\partial}{\partial x} \vec{e}_x + \frac{\partial}{\partial y} \vec{e}_y$ is the horizontal gradient operator. In addition, the ocean can exchange momentum with the solid Earth through frictional processes across a small

boundary layer. The friction is parameterized as turbulent fluxes ($\overline{D_u}$) for the bottom and lateral boundary conditions because the grid mesh is not fine enough to explicitly resolve such a layer. Nonlinear quadratic bottom friction is used in the model.

Ocean-atmosphere boundary: The ocean-atmosphere interface exchanges horizontal momentum via wind forcing, heat flux via solar and longwave radiation, and freshwater flux via precipitation and evaporation. The ocean surface is a linear free surface, where the SSH changes in time but the thickness of the first vertical level is fixed. The dynamic boundary condition is governed by the kinematic surface condition plus the freshwater flux, which is expressed as:

$$w = \frac{\partial \eta}{\partial t} + \vec{u}|_{z=\eta} \cdot \nabla_z \eta + P - E \quad (2.12)$$

where P and E represent precipitation and evaporation respectively. This dynamic boundary condition leads to the continuity of pressure across the surface $z = \eta$.

The wind affects the momentum by exerting a force over the sea surface. The wind forcing is the chief source of momentum onto the ocean. The surface wind stress is computed from the Coordinated Ocean-ice Reference Experiments (CORE) bulk formulae:

$$\tau_{wo} = \rho_a C_o |\Delta U_{wo}| \Delta U_{wo} \quad (2.13)$$

Where

τ_{wo} is the surface wind stress,

ρ_a is the density of the air (1.22 kg/m^3),

C_o is the transfer drag coefficient for the ocean,

ΔU_{wo} is the velocity difference between the wind and surface ocean current.

The Ekman transport is the net transport of the resulting flow arising from the surface wind stress. Persistent wind stress sets surface seawater adrift and generates the Ekman spiral within a thin layer. The integrated flow over the Ekman layer is expected to be 90° to the right of the wind direction in the Northern Hemisphere due to Coriolis deflection under ideal circumstances (steady forcing and large depth).

$$D_{Ek} = 0.70 * \left(\frac{1}{f} \sqrt{\frac{\tau_{wo}}{\rho_o}} \right) \quad (2.14)$$

$$f = 2\Omega \sin(\phi) \quad (2.15)$$

$$\tau_{wo} = \sqrt{\tau_x^2 + \tau_y^2} \quad (2.16)$$

$$T_{Ek}^x = \frac{\tau_y}{f\rho_o} dy \quad (2.17)$$

$$T_{Ek}^y = -\frac{\tau_x}{f\rho_o} dx \quad (2.18)$$

$$T_{Ek} = \sqrt{T_{Ek}^x{}^2 + T_{Ek}^y{}^2} \quad (2.19)$$

Where

D_{Ek} is the depth of the Ekman layer,

f is the Coriolis parameter,

ϕ is the latitude,

τ_x and τ_y are the wind surface stress in x and y directions, respectively;

T_{Ek}^x and T_{Ek}^y are the Ekman transport in the x and y directions of the model grid, respectively and T_{Ek} is the total Ekman transport.

dx and dy are the length of each model grid cell in x and y directions, respectively;

ρ_o is the reference density of the seawater (1,030 kg/m³).

Shear in the surface wind stress eventually leads to an Ekman upwelling or Ekman downwelling. The wind stress shear can be defined by the wind stress curl. The vertical component of the wind stress curl is given by

$$(\nabla \times \tau_{wo}) \cdot \vec{e}_z = \frac{\partial \tau_y}{\partial x} - \frac{\partial \tau_x}{\partial y} \quad (2.20)$$

And the vertical velocity of the Ekman upwelling or Ekman downwelling is thus described as

$$w_{ek} = \frac{1}{\rho_o f} (\nabla \times \tau_{wo}) \cdot \vec{e}_z \quad (2.21)$$

The ocean and atmosphere exchange heat fluxes through turbulent processes. The net surface heat is composed of the shortwave and longwave radiation, and the latent and sensible heat fluxes. Each term is derived from CORE bulk formulae:

$$Q = Q_{sw} + Q_{LW} + Q_L + Q_S \quad (2.22)$$

$$Q_{SW} = Q_I(1 - \alpha) \quad (2.23)$$

$$Q_{LW} = Q_D - \sigma T_o^4 \quad (2.24)$$

$$Q_L = \rho_a L_v C_e (q_a - q_o) |\Delta U_{wo}| \quad (2.25)$$

$$Q_S = \rho_a C C_h (T_a - T_o) |\Delta U_{wo}| \quad (2.26)$$

Where

Q is the net surface heat, Q_{SW} is the net shortwave heat flux, Q_{LW} is the net longwave heat flux,

Q_L is the latent turbulent heat flux, and Q_S is the sensible turbulent heat flux;

Q_I is the solar insolation on the ocean surface, Q_D is the incident downwelling longwave radiative flux on the ocean surface,

α is the surface albedo,

ϵ is the emissivity, σ is the Stefan-Boltzmann constant ($\sigma = 5.67 \times 10^{-8} W m^{-2} K^{-4}$);

ρ_a is the density of the air ($1.22 kg/m^3$);

L_v is the latent heat of vaporization ($2.5 \times 10^6 J kg^{-1}$),

C is the specific heat of the air ($1000.5 J kg^{-1} K^{-1}$),

T_a and T_o denote the potential air temperature at $z = 10 m$ and the sea surface temperature respectively, both in Kelvin,

q_a is the specific humidity of the air at $z = 10 m$,

q_o is the saturated specific humidity at T_o .

ΔU_{wo} is the velocity difference between the wind and surface ocean current

C_e and C_h are the latent and sensible transfer drag coefficients respectively (Large & Yeager, 2009).

Ocean-sea ice boundary: Exchanges of heat, salt, and momentum take place at the ocean-sea ice interface. Underneath the sea ice, the sea surface temperature is constrained to be at the freezing point (0 °C) at the interface. The sea surface salinity has a strong seasonal cycle in high latitude ocean associated with the sea ice freezing and melting. The forming of the sea ice causes brine rejection, leading to a positive salt flux into the ocean. As the sea ice melts, whose salinity (~4 – 6) is far lower than the seawater (~34), it significantly reduces the sea surface salinity below the sea ice and results in a negative salt flux. Other than the thermodynamic effects, it also has mechanical consequences for the dynamics through the momentum transfer into the ocean. Momentum fluxes are regulated by the friction if the sea ice is land-fast or by the stress if the sea ice is moving around. The surface stress from sea ice is again computed from the CORE bulk formulae.

$$\tau_{io} = \rho_o C_i |\Delta U_{io}| \Delta U_{io} \quad (2.27)$$

Where

τ_{io} is the surface stress due to sea ice,

ρ_o is the reference density of the seawater (1,030 kg/m³),

C_i is the transfer drag coefficient for the ice,

ΔU_{wo} is the velocity difference between the drifting sea ice and surface ocean current.

2.3 Grid structure

Due to the convergence of the meridians on a spherical Earth, which induces a singularity point at the North pole, a regular latitude-longitude grid on the geographical coordinate system cannot be used in the model horizontal mesh. A solution is to reconstruct to have a tri-polar grid on the

orthogonal curvilinear coordinate system (Figure 2.1). It transforms the singular point at the North pole into two geometric poles with one over Canada and the other over Russia. The tri-polar grid does not have a uniform grid spacing and regularly spaced lines. The regional configuration of NEMO used in this thesis, Arctic and Northern Hemisphere Atlantic (ANHA), has a resolution of $1/4^\circ$ and a finer resolution of $1/12^\circ$ (Figure 2.2). Their model grid meshes are extracted from the corresponding global ORCA tripolar grids. Both of them have two open boundaries with one near the Bering Strait and the other at 20°S in the South Atlantic Ocean. A staggered Arakawa C-grid for spatial discretization and numerical algorithms is widely used in NEMO due to its favourable conservation properties (Mesinger & Arakawa, 1976), whereby the variables are stored at different points in the unit cell of the space domain (Figure 2.3). Scalar variables like temperature (T), salinity (S), pressure (p), and density (ρ) are displayed on the red T points; Meridional (v), zonal (u) and vertical (w) velocities are located on the green V points, blue T points and purple W points, respectively; The relative vorticity (ζ), planetary vorticity (f) and the barotropic stream function (ψ) are represented at the gold F points. All the points have a specific integer indexing to be computed in the code. The arrangement of variables is consistent in the three directions. The skeleton of the model grid is defined by two horizontal scale factors (e_1 , e_2) and a vertical scale factor (e_3) (Madec 2016).

The vertical coordinate of the model is divided into levels with a fixed thickness on a z-coordinate. Vertical spacing is not linear either, with a fine resolution near the sea surface and a coarser resolution at depth. Therefore, the spatial features on the upper ocean (top 1000 m) are more accurately resolved. The bathymetry product determines the structures of the seafloor and coast. The representation of the bottom topography and continental shelf and slope has greatly improved by applying a partial step method (Bernard et al., 2006). While keeping the advantages of the

traditional z -coordinate, the thickness of the bottom layer could vary as a function of geographical location, so that it is closer to the average depth of the topography (Figure 2.4).

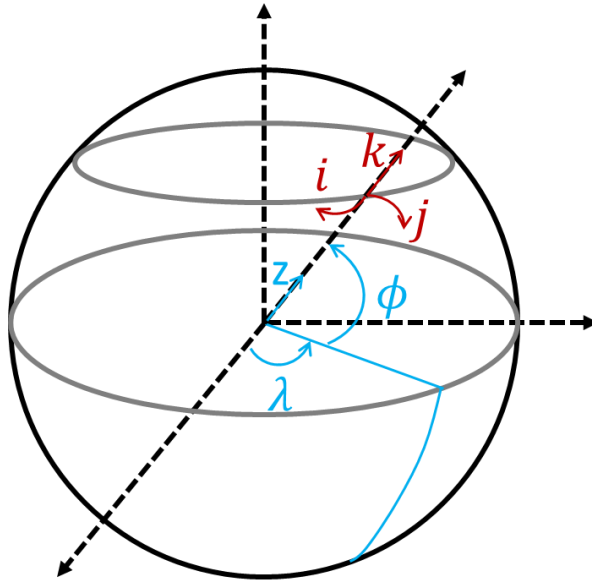


Figure 2.1 The geographical coordinate system (λ, ϕ, z) and the curvilinear coordinate system (i, j, k). λ and ϕ are aligned with the Earth's longitudes and latitudes respectively. i and j represent the zonal and meridional direction of the horizontal model grid respectively. z and k point in the same direction that is perpendicular to the horizontal panel (geopotential surfaces of the spherical Earth).

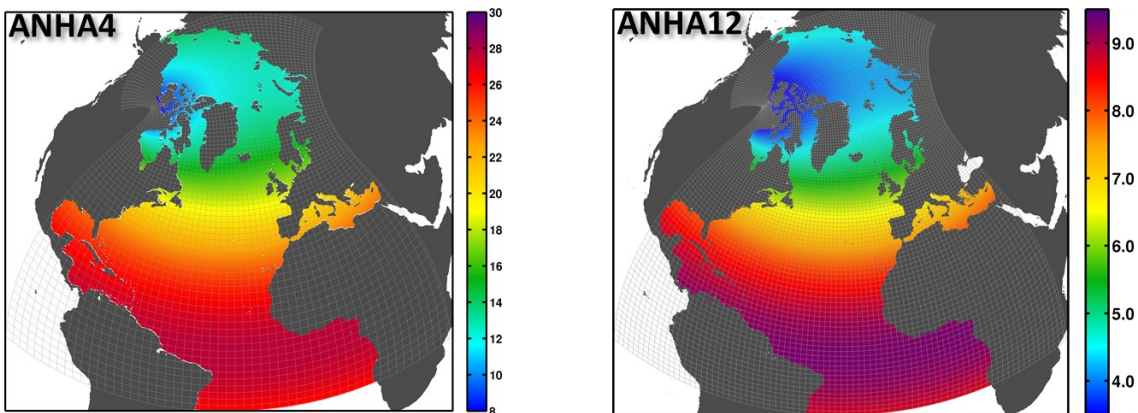


Figure 2.2 The horizontal mesh of ANHA4 and ANHA12 (colour shows the resolution in kilometres). The singular point is removed from the North Pole, and two new geometric poles are located at Dease Strait and Siberia separately.

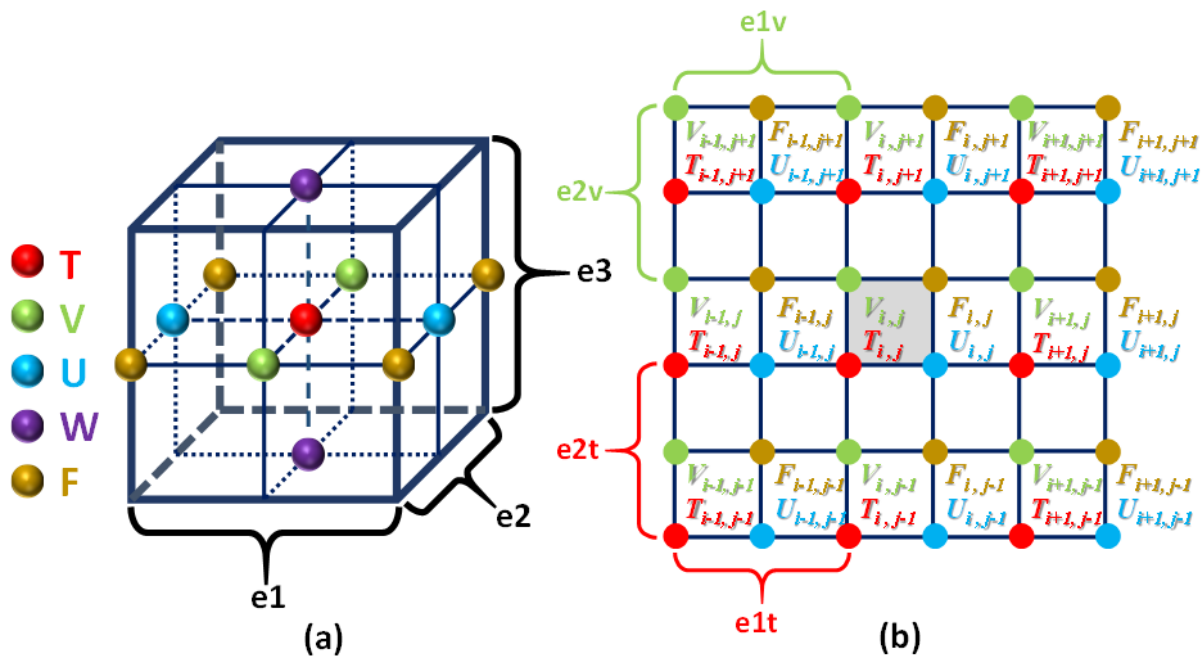


Figure 2.3 3D cabinet perspective (a) and 2D top-down view (b) of the variable arrangement in the NEMO mesh grid (Arakawa C-grid). The red T point in the cell center represents scalar points; The green V points, blue T points and purple W points in the center of each face indicate vector points; The gold F point in the center of each vertical edge stands for vorticity points. Three scale factors (e_1 , e_2 : horizontal; e_3 : vertical) define the size of each grid cell in (a). Horizontal integer indexing has been chosen as shown in (b). The T, V, U, and F points having the same i - and j -indices are indicated by the dashed square. e_{1t} , e_{2t} is the length of the T grid cell in the horizontal plane, and so on.

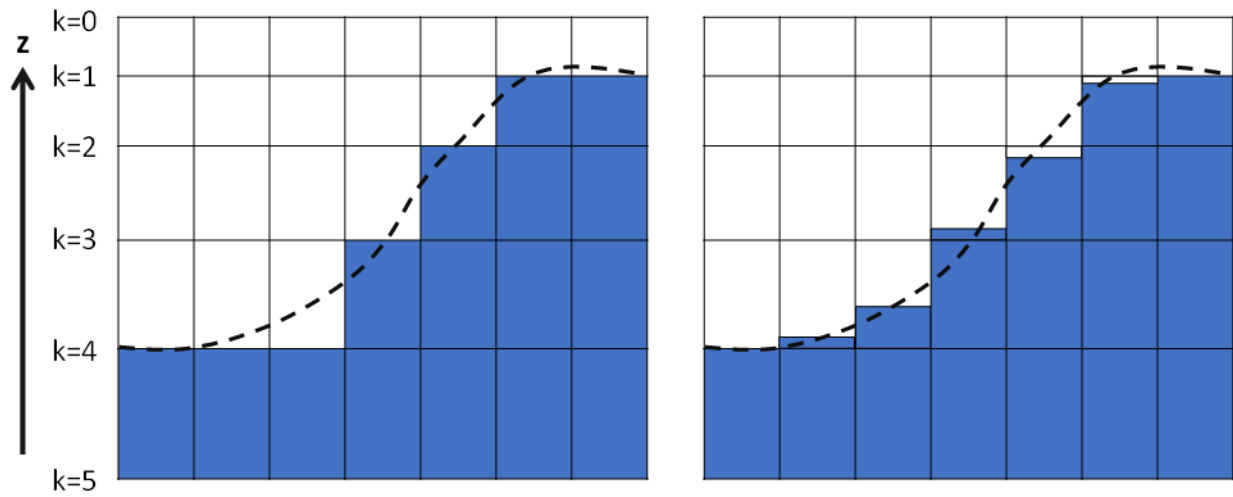


Figure 2.4 Vertical model grid with the traditional full step z-coordinate (left), and partial step with z-coordinate (right). Shaded cells represent the model bottom bathymetry and the dashed lines show the real sea floor.

3. Pulses of Cold Atlantic Water in the Arctic Ocean from Ocean Model Simulation

Abstract

Atlantic Water (AW) is a warm and salty water mass that distinguishes itself from the cold and fresh Arctic Water. The AW flows into the Arctic Ocean in two branches, Fram Strait Branch Water (FSBW) and Barents Sea Branch Water (BSBW). Numerical modelling is an effective tool to simulate the AW based on its thermohaline properties. We first evaluate the interannual and seasonal variability of the AW thermohaline structure at these two gateways, then quantify the AW volume and heat transport on the interannual and seasonal timescales. We also compare long-term transport means with the available observations. We discover two strong Cold Atlantic Water (CAW) anomaly events along the rim of the eastern Eurasian Basin in 2013 and 2014, overturning our understanding that the AW is always warm and saline. The dominant contributor to the CAW formation is the intense sea surface cooling in the Barents Sea for two consecutive years. Releasing artificial particles at Fram Strait and the BSO, we find that the source of the CAW is primarily from the BSBW. The CAW signals progress along the typical AW poleward pathway and eventually reduce the heat that is contained in the AW layer of the eastern Arctic Basin.

3.1 Introduction

The Arctic Ocean resembles an isolated Mediterranean Sea. Two deep basins, divided by the Lomonosov Ridge, sit at the centre: the Canadian and Eurasian Basins with average depths of roughly 4000 m (Figure 3.1). Shallow continental shelves are found on the periphery defining the Arctic marginal seas (Figure 3.1). Other than receiving the freshwater from river runoff from the surrounding landmasses and more precipitation than evaporation, it also receives Pacific-origin inflow (Pacific Water, hereafter PW) via Bering Strait and Atlantic-origin inflow (Atlantic Water, hereafter AW) through Fram Strait and the Barents Sea Opening (BSO). AW is a typically warm and saline water mass that originates from the Northern Atlantic Ocean. Therefore, these two AW branches, carrying the Fram Strait Branch Water (FSBW) and the Barents Sea Branch Water (BSBW), transport a great amount of heat and salt into the cold and relatively fresh Arctic Ocean. The AW forms an intermediate layer (~200-1000 m) in the Arctic basins with a maximum temperature of up to about 1°C, fed by the warm and salty FSBW and the relatively cool and less saline BSBW. The BSBW mixes with and partially subducts below the warm core of the FSBW (Pérez-Hernández et al., 2019; Li et al., 2020). For the upper layer, the surface mixed layer is thin, with a normal thickness of 5-10 m throughout the Arctic Ocean (Woodgate, 2013). Unlike the Canadian Basin which has a stronger stratification, in the Eurasian Basin, there is no PW band but a thicker cold Atlantic halocline. The halocline separates the AW layer from the surface mixed layer and limits the vertical heat flux from the warmer AW layer to the surface mixed layer. Below the AW layer is the cold and saline Arctic Bottom Water (Woodgate, 2013). The water density of the Arctic Ocean is mainly determined by the salinity based on the non-linear equation of state, so salinity changes have a more profound impact on modifying the stratification than ocean temperature changes (Carmack, 2007). However, the thermodynamic impact is amplifying as the

Arctic has been warming under the effect of global warming and Arctic amplification. According to model studies and observations, the oceanic heat transport to the Arctic Ocean via AW through Fram Strait and the BSO has increased during recent decades (Beszczynska-Möller, 2012; Muilwijk et al., 2018; Spielhagen et al., 2011; Wang et al., 2019, 2020). The Arctic Ocean has demonstrated a rapid downward trend of minimum sea ice cover at the end of the summer for the last several decades (Cavalieri & Parkinson, 2012; Comiso, 2012; Comiso et al., 2017; Stroeve et al., 2007), and has shown an ongoing acceleration in the decline of the Arctic sea ice cover (Cavalieri & Parkinson, 2012; Stroeve et al., 2007). They also diagnose a thinning of the average Arctic multiyear ice cover (Comiso, 2012; Spreen et al., 2020). All these signs indicate a warming world and the possibility of an ice-free Arctic Ocean (less than 10^6 km²) in summer as early as 2030-2050 (Guarino et al., 2020).

Fram Strait is one of the Arctic gateways, between Greenland and Svalbard. It is one of two important sections for evaluating the variability of the AW entering the Arctic Ocean (Beszczynska-Möller, 2012). The warm and salty AW that flows into the Arctic Ocean is carried by the northward-flowing West Spitsbergen Current (WSC) through Fram Strait. Some portion of the AW recirculates back to the south through several recirculation pathways south of 81°N and mostly subducts underneath the Arctic Water (ArW) advected by the southward flowing East Greenland Current (EGC). This is primarily achieved by the spawning of the abundant mesoscale eddies (with the Rossby radius of deformation of 3-6 km) near Fram Strait (Wekerle et al., 2020). The AW flowing into the Arctic Basin through Fram Strait splits into three major pathways: the shallow Svalbard Branch along the Svalbard continental slope at 400-500 m depth (~0.8 Sv), the Yermak Pass Branch that flows across the Yermak Plateau at 700-800 m depth (~1.9 Sv), and a relatively minor component comprising the deep Yermak Branch following the western slope of

the Yermak Plateau along ~1000 m isobath (~0.1 Sv) (Crews et al., 2019; Menze et al., 2019; Pérez-Hernández et al., 2019). These three branches vary on the seasonal and interannual time scales. Ultimately, they merge east of the Yermak Plateau and form the FSBW that flows along the rim of the Eurasian Basin (Athanasé et al., 2020). The AW is cooled and freshened near Fram Strait through a suite of processes such as the sea ice melt, winter convection, lateral eddy fluxes as well as exchanges with shelf waters and trough outflows (Athanasé et al., 2020; Rudels et al., 2015). Kawasaki and Hasumi (2016) studied the AW inflow at the Fram Strait by using an ice-ocean model and provided a quantitative analysis of the heat transport. According to their findings, the heat flux is lost through: (I) transporting westward (47%); (II) sea surface cooling (16%); (III) injection into the Arctic Ocean interior (37%). They reported that the interannual variability of heat transport toward the Arctic Ocean has strong links to the Sea Level Pressure (SLP) variability modulated by the NAO index.

The Barents Sea is a marginal sea of the Arctic Ocean with a rather shallow continental shelf (average depth ~250 m). The BSO is a hydrographic gateway between Bear Island and the northern end of Norway at the western boundary of the Barents Sea. It is another route, although a shallow one, for the AW entering the Arctic Ocean. After passing through the Norwegian Sea, the AW splits from the Norwegian Atlantic Current (NAC) and then enters the Barents Sea through the BSO. The circulation of the AW in the Barents Sea is greatly confined by the regional bathymetry, especially the shallow area (Oziel et al., 2016). The southern and central parts of the Barents Sea are permanently sea-ice free, so the AW is exposed to the air directly and experiences substantial sea surface cooling. When the AW reaches the northern Barents Sea, which is normally ice-covered during winter, its heat is further lost by interacting with the sea ice (Rudels et al., 2015; L H Smedsrud et al., 2010). The winter sea ice cover reduction in the northern and eastern Barents Sea

has become particularly pronounced since 1979 (Onarheim & Årthun, 2017), thus the coupling between the atmospheric forcing and the ice-free ocean has been enhanced in these regions. The Barents Sea has become a key area for the water mass transformation induced by the surface buoyancy fluxes. The heat transport through the BSO is closely related to the amount of volume transport and the inflow temperature. It is the most crucial heat supply to the Barents Sea that helps maintain its largely ice-free ocean status. Mechanisms interfering with the interannual variability of the heat transport through the BSO are explained by Wang et al., (2019). They state that half of the variability is caused by the local wind forcing which contributes to the variation in volume transport by changing the Sea Surface Height (SSH) gradient across the BSO. The other half is controlled by the wind and buoyancy forcing from upstream as a result of the changes in both the volume transport and temperature.

As the FSBW and BSBW meet and mix at the St. Anna Trough (SAT), the merged AW boundary current (AWBC) continues to flow along the continental margin of the Eurasian Basin cyclonically. When the boundary current reaches the Lomonosov ridge, where the section we call S3 is located (Figure 3.1), it bifurcates into two branches. We define section S4 to document the flow progressing along the ridge, while section S6 keeps track of the portion continuing into the Canadian Basin (Figure 3.1). The AWBC is strongly topographically steered, following around bathymetric contours in the Arctic Basin. Timmermans & Marshall, (2020) discussed the controlling mechanisms of the circulation from two perspectives: one is from buoyancy-driven processes based on a double-layer estuary framework, with the ArW in the upper layer and AW below. The AW inflow is driven by the freshwater input, PW inflow flux, and the AW entrainment and mixing between two layers; the other perspective is from wind-driven flow along potential vorticity contours that is regulated by seafloor topography. It is set by the anticyclonic wind stress

in the Beaufort Gyre region and the cyclonic atmospheric forcing in the Nordic Seas. Mooring observations indicate that the AWBC speed decreases gradually from ~ 20 cm/s near Fram Strait to ~ 4 cm/s at the Lomonosov Ridge, with the baroclinic nature of the flow in the vertical structure becoming dominated en route (Pnyushkov et al., 2015). The encroachment of the warm and saline AW into the Arctic Ocean refers to “Atlantification” and potentially changes the atmospheric and oceanic circulations, vertical structure, and sea ice conditions in the Arctic Ocean. The geostrophic AW volume transport decreases by about one order of magnitude during its progression along the continental slope of the Arctic Basin between the inflow Arctic gateways and the Makarov Basin (Zhurbas & Kuzmina, 2020). This is accompanied by the weakening of the seasonal signal amplitude in the current speed variability and AW temperature (Pnyushkov et al., 2015). The AW layer will be extensively modified in the warm climate scenario when the local sea ice cover has decreased or the properties of the transported FSBW and BSBW have changed. Polyakov et al., (2017) proposed that sea ice has retreated significantly to the eastern Eurasian Basin owing to the increased AW at mid-depth, which favours surface heat loss to the atmosphere and renders strong local winter ventilation. The surface heat loss is thus supported by the enhanced upward heat transfer from the AW layer. The circumstance of how the changes in FSBW and BSBW affect the AW layer will be later discussed in this paper.

The paper is structured as follows: Section 3.2 describes the model simulations and introduces the methods and approaches that we use in the analysis. Section 3.3.1 gives a census of the water masses at Fram Strait and the BSO in the model with a focus on the thermohaline structure and strength of the FSBW and BSBW. Section 3.3.2 assesses the temporal variability of the AW volume and heat transport at Fram Strait and the BSO, and also compares the mean state over 2011-2019 from the simulated results and the observations. Section 3.3.3 covers the AW’s poleward pathways

from the FSBW and BSBW within the Arctic Ocean. In Section 3.3.4, we introduce the CAW that is below the standard temperature range and propose its sources. We then further analyze the transformation rate exerted from surface heat and freshwater fluxes to investigate the driving mechanisms of CAW formation in Section 3.3.5. Lastly, Section 3.4 concludes the study and discusses its limitations.

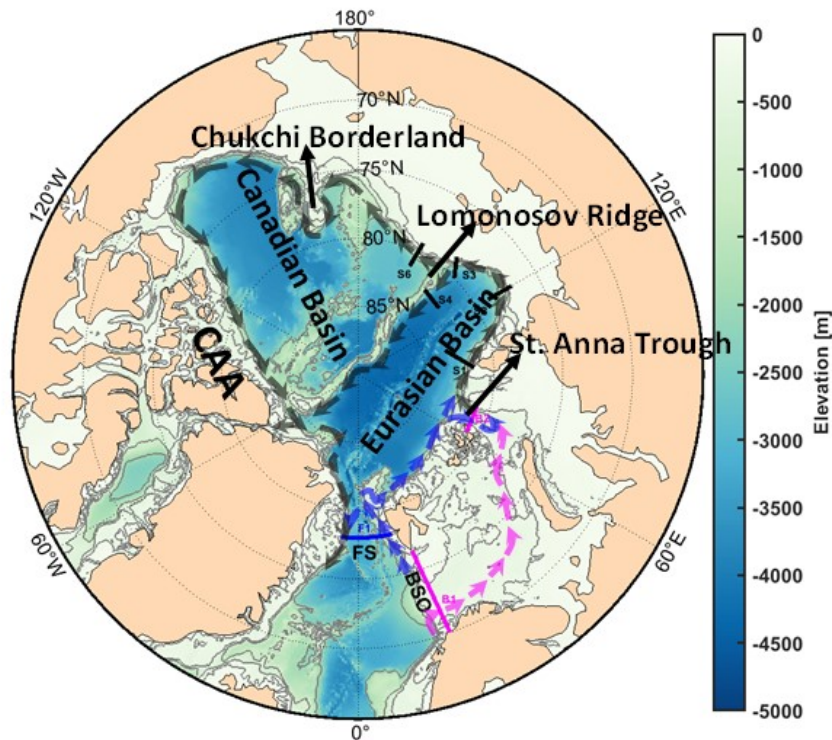


Figure 3.1 The schematic of the large-scale circulation pattern of the Atlantic Water inflow to the Arctic Ocean, with major geographic features labelled. The blue, magenta, and black lines composed of arrows represent the FSBW, BSBW, and AWBC respectively. The locations of the Arctic gateway straits (F1 and B1) and sections along the poleward pathway (B2, S1, S2, S3, S4 and S6) are indicated. Contour lines are -200 m, -500 m, -1000 m and then -2000 m. FS: Fram Strait, BSO: Barents Sea Opening, CAA: Canadian Arctic Archipelago.

3.2 Numerical Methods

3.2.1 Numerical Model Description and Setup

In this study, a state-of-art modelling framework called Nucleus for European Modelling of the Ocean (NEMO) version 3.4 is used. It includes a three-dimensional, eddy-permitting and primitive-equation ocean general circulation model Océan PARallélisé (OPA), and the sea ice model Louvain-la-neuve Ice Model version 2 (LIM2) with a modified elastic-viscous-plastic ice rheology, and has thermodynamic and dynamic processes (Fichefet & Maqueda, 1997; Hunke & Dukowicz, 1997; Madec, 2016).

A regional configuration of the interactively coupled ocean-sea ice model covering the Arctic and the Northern Hemispheric Atlantic (ANHA) is applied to carry out the numerical simulations. Two different resolutions of the configuration are used. The model grid mesh has an eddy-permitting resolution of $1/4^\circ$ (hereafter ANHA4, 544×800 grid points at each vertical level) and a $1/12^\circ$ configuration (hereafter ANHA12, 1632×2400 grid) (Hu et al., 2019), extracted from the corresponding global ORCA tripolar grids. In ANHA12, the finest grid spacing is ~ 1.9 km in Dease Strait, close to the artificial pole over northern Canada, while the coarsest grid spacing is ~ 9.3 km at the equator. The horizontal resolution at Fram Strait and the BSO is close to 4 km, and around 13 km in ANHA4. There are 50 geopotential vertical levels with the maximum ocean depth at 5727.92 m. Higher vertical resolution is applied to the upper ocean (< 2 m resolution for top 10 m) with layer thickness increasing non-linearly from 1.05 m at the surface to 453.14m at the last level. The bathymetry for the Arctic Ocean region stems from the 1 arc-minute global relief model of

Earth's surface (ETOPO1) built from the NOAA dataset, and the bottom topography (seafloor) is significantly improved by using partial steps (Bernard et al., 2006).

The integration of the ANHA12 simulation starts from January 2002 to the end of December 2019 with 5-day average output. The timespan of 2011-2019 is chosen for our analysis to avoid the model spin-up. The initial conditions, including 3D ocean fields (temperature, salinity, zonal and meridional velocities) as well as 2D sea surface height and sea ice fields (sea ice concentration and thickness), are obtained from the GLobal Ocean ReanalYsis and Simulations 2 version 3 (GLORYS2v3) produced by Mercator Ocean (Masina et al., 2017). There are two open boundaries for the configuration, one is close to Bering Strait in the Pacific Ocean and the other one aligns at 20°S across the South Atlantic Ocean. Monthly open boundary conditions (temperature, salinity and horizontal ocean velocities) are also derived from the GLORYS2v3 dataset. The high temporal (hourly) and spatial (33 km) resolution atmospheric forcing acting on the sea surface, including 10-m surface wind, 2-m air temperature, specific humidity, total precipitation as well as surface downwelling shortwave and longwave radiative fluxes, are taken from the Canadian Meteorological Centre's (CMC) Global Deterministic Prediction System (GDPS) ReForcasts (CGRF) dataset (Smith et al., 2014). The baroclinic model time step is 180s for ANHA12 and 1080s for ANHA4. No temperature and salinity are restored so that the output represents the physical processes of the ocean model. The global monthly river discharge data ($1^\circ \times 1^\circ$) from Dai et al. (2009) and the interannual monthly Greenland meltwater data ($5 \text{ km} \times 5 \text{ km}$) provided by Bamber et al. (2012) are remapped onto the model grid. The river runoff dataset is from Global River Flow and Continental Discharge Dataset (Dai & Trenberth, 2002). Tides are not taken into consideration in the numerical experiments except for Video 1 in the supplementary material where

we use the updated version of ANHA4 (Table 3.1). The updated ANHA4 is based on NEMO 3.6, a successor of NEMO 3.4. It also uses the HYdrological Predictions for the Environment (HYPE) modelled runoff dataset that covers both major rivers and local runoff (Stadnyk et al., 2021).

Table 3.1 NEMO Experiments using the ANHA configuration.

Simulation	ANHA12-EXH006	ANHA4-EXH015	ANHA4-ECF002
Ocean Model	NEMO 3.4	NEMO 3.4	NEMO 3.6
Integration	2002-2019	2002-2016	2002-2019m06
Sea Ice Model	LIM2	LIM2	LIM2
Initial Condition	GLORYS2v3	GLORYS2v3	GLORYS2v3
Open Boundary Condition	GLORYS2v3	GLORYS2v3	GLORYS2v3
Atmospheric Forcing	CGRF	CGRF	CGRF
Runoff	Dai and Trenberth runoff and Greenland melt	Dai and Trenberth runoff and Greenland melt	HYPE
Tides	No	No	Yes
Output	5-day NORMAL	5-day NORMAL	5-day NORMAL

3.2.2 Ariane and Online Passive Tracers

Ariane is a practical offline particle-tracking software package using the Lagrangian method (Blanke, 2002), which is helpful to explore the large-scale ocean circulation of a particular water mass at a fairly low computational cost. Unlike the application of the online passive tracers, it avoids running multiple model simulations. We compute the 3D particle trajectories changing with time using Ariane from a modelled ocean velocity field so that we can track the Atlantic inflow

and analyze its paths. Each particle retains its infinitesimal volume over the course of the integration. Although dynamic processes such as diffusion and convective mixing cannot be represented from the Lagrangian tracking, the Eulerian output fields from the ocean model have included these effects and the temperature, salinity and density of each particle evolve based on such fields (Kelly et al., 2018). Therefore, Ariane should produce a reliable representation of the particle pathways. Here, the release of the virtual particles is based on the fields provided by the ANHA12 output. The calculation of how many particles to release in each grid cell is according to this formula.

$$n = N \times \frac{V}{V_{total}} \times \frac{v}{v_{mean}} \quad (3.1)$$

where n is the number of the particles in an identified grid cell along the sections (FS, BSO, and B2) and N is the sum of all the particles at each identified grid cell; V is the volume of each identified grid cell (m^3) and V_{total} is the total volume of identified grid cells (m^3); v is the velocity of each identified grid cell (m/s) and v_{mean} is the mean velocity of all the identified grid cells (m/s). The grid cell is identified when it meets the thermohaline criteria of the AW or the CAW defined for that section and has a positive velocity indicating flowing toward to the Arctic Ocean.

Following the method from Hu et al., (2019), online passive tracers are applied to trace the AW inflow to the Arctic Ocean from Fram Strait and the BSO, starting from January 1, 2002. Since online passive tracers are embedded in the ocean model, the dynamical processes are well resolved, so that it can represent the pathway of the water mass more accurately. The passive tracer concentration is a non-dimensional quantity as a ratio of the volume of a water mass entering a grid cell over the volume of the grid cell, so an increment ΔC is proportional to the amount of the volume flux:

$$\Delta C = \frac{e1v \cdot e3v \cdot v}{e1t \cdot e2t \cdot e3t} dt \quad (3.2)$$

then the vertically integrated tracer concentration could be described as:

$$Cv = \int_z^0 \Delta C(x, y, z, t) dz \quad (3.3)$$

where $e1v$ is along-section grid length (m), $e3v$ is the corresponding grid cell thickness (m), v is the velocity perpendicular to the section (m/s), dt is model time step (s), $e1t$, $e2t$ and $e3t$ are the grid length scales for T grid points (m), z is the largest depth that tracers could reach. Like the Ariane tracers above, these passive tracers are released if they are in the AW temperature and salinity ranges, and their velocity is towards the Arctic Ocean.

3.2.3 Transport and Content Calculations

The volume and heat transport and freshwater and heat content can be computed from the 5-day mean output from the numerical model as follows:

The volume transport (Sv, $1Sv = 10^6 m^3/s$):

$$T_{Vol} = \int_0^S v_i dS = \iint_{-D}^0 v_i dl dz \quad (3.4)$$

The heat transport (kW or kJ/s):

$$T_H = \int_0^S v_i \rho_o C_p (\theta_i - \theta_{ref}) dS = \iint_{-D}^0 v_i \rho_o C_p (\theta_i - \theta_{ref}) dl dz \quad (3.5)$$

where v_i is the cross-strait seawater velocity at each model grid cell (m/s), dS is the differential area of the section (m^2), dl is the differential length of the section (m), dz is the differential depth (m), θ_i is the seawater potential temperature ($^{\circ}C$), θ_{ref} is the reference temperature ($0^{\circ}C$); ρ_o is

the reference density of the seawater ($1,030 \text{ kg/m}^3$), C_p is the specific heat capacity of the seawater ($4.0 \times 10^3 \text{ J/kg} \cdot ^\circ\text{C}$).

The freshwater content (m^3):

$$V_{FW} = \int_0^V \left(\frac{S_{ref} - S_i}{S_{ref}} \right) dV = \iint_{-D}^0 \left(\frac{S_{ref} - S_i}{S_{ref}} \right) dAdz \quad (3.6)$$

The heat content (kJ):

$$H = \int_0^V \rho_o C_p (\theta_i - \theta_{ref}) dV = \iint_{-D}^0 \rho_o C_p (\theta_i - \theta_{ref}) dAdz \quad (3.7)$$

where S_{ref} is the reference salinity (34.8), dV is the differential volume of the domain, dA is the differential area of the horizontal domain (m^2). D is the largest depth of the domain (m).

3.2.4 Air-Sea Transformation Estimates

Adapting from Myers & Donnelly, (2008) and Petit et al., (2020) that are based on an approach originally presented in Speer & Tziperman, (1992), we come up with an approach to quantify the transformation to the CAW based on its temperature and salinity characteristics ($T < 0^\circ\text{C}$, $S > 34.8$).

The transformation is in response to the forcings from the surface heat and freshwater fluxes.

$$F(\sigma^*) = \frac{1}{\Delta\sigma} \iint \left[-\frac{\alpha}{C_p} Q + \rho\beta SH \right] \Pi(\sigma, T, S) dx dy \quad (3.8)$$

$$\Pi(\sigma) = \begin{cases} 1 & \text{for } |\sigma - \sigma^*| \leq \frac{\Delta\sigma}{2}, T < 0, S > 34.8 \\ 0 & \text{elsewhere} \end{cases} \quad (3.9)$$

where α is the thermal expansion coefficient, β is the haline contraction coefficient, C_p is the specific heat capacity, Q is the net surface heat flux into the ocean, which is a combination of the shortwave and longwave radiation, and the sensible and latent heat fluxes ($Q = Q_{SW} + Q_{LW} +$

$Q_L + Q_S$), H is the net surface freshwater flux that comes from evaporation minus precipitation (E-P). We do not take sea ice melting and freezing into account because while it may impact the surface water properties, salinity in particular, it will not directly transform the waters. The runoff discharge only produces a transformation to a less dense water mass and mainly takes effect in summer, so it is neglected in our calculation. ρ is the surface density, S is the surface salinity, σ is the surface density anomaly ($\rho - 1000$), σ^* is the middle value of the density bin and $\Delta\sigma$ is the width of the density bin that is set at $\Delta\sigma = 0.05 \text{ kg/m}^3$ taking into account both resolution and noise (Speer & Tziperman, 1992).

We diagnose evaporation (E) via the specific humidity at the sea surface and compare it against the specific humidity of the air. It is computed from the Coordinated Ocean-ice Reference Experiments (CORE) bulk formulae (Large & Yeager, 2009). Precipitation (P) is comprised of snowfall and rain that is directly derived from the atmospheric forcing dataset CGRF. The transformation rate at a particular density bin represents the volume of the water mass that transforms to denser water mass, or less dense water mass, depending on the sign. Surface buoyancy fluxes produce transformation when the surface density is within the density bin, and the temperature and salinity also meet the criteria for the CAW. In our simulation, more dense water being formed would represent an increase in the CAW formation.

3.3 Results

3.3.1 Thermohaline Structure of the AW at Fram Strait and the BSO

We first evaluate the hydrographic properties (temperature, salinity and cross-section velocity) of the model water masses at Fram Strait and the BSO in the chosen year of 2013, as shown in Figure 3.2 (the rationale for choosing this year will be revealed in section 3.4). At Fram Strait, the

modelled temperature and velocity fields generally coincide with the observational measurements by the mooring arrays from Beszczynska-Möller et al, (2012). The thermohaline structure of water masses at Fram Strait is characterized by the warm and saline AW inflow at the eastern shelf and cold and fresh Arctic Water outflow on the other side. Both have the temperature and salinity cores along the shelf near the surface with the annual mean velocity cores exceeding 10 cm/s. Compared to the Arctic Water outflow, the AW inflow is less baroclinic so that the velocity core reaches deeper to a depth of near 700 m. The temperature and salinity fields demonstrate a similar contour pattern and the temperature and salinity cores extend further to the west in the strait. The AW recirculation branches, which are considered as return flows of the WSC offshore branches, can be observed in the central Fram Strait from the cross-section velocity plot (Figure 3.2c). The bulk AW recirculation is driven by the seasonally varying mesoscale eddy activity (Hattermann et al., 2016). The drastic lateral density gradient between these two water masses potentially enhances the baroclinic instability at Fram Strait and thus greatly catalyzes the abundant eddy generation (Wekerle et al., 2020).

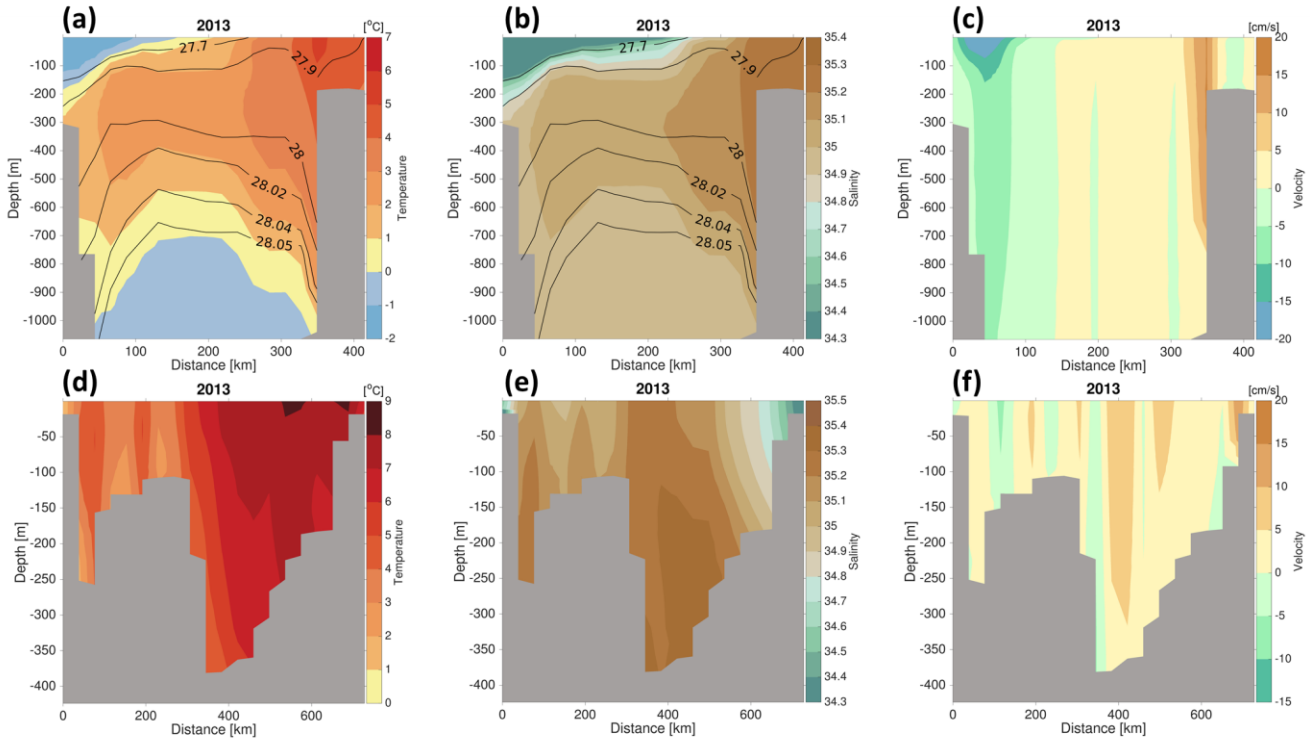


Figure 3.2 Annual mean temperature T (a & d, unit: $^{\circ}\text{C}$), salinity S (b & e), and normal to cross-section velocity v (c & f, unit: cm/s) at Fram Strait (Upper panels) and the BSO (Lower panels) in 2013. The velocity is positive towards the Arctic Ocean. The isopycnal lines are contoured onto the temperature and salinity fields in Fram Strait. The x-axis shows the distance (Fram Strait: from west to east; BSO: from north to south) in kilometres and the y-axis shows the ocean depth in metres.

We define the AW as having a temperature greater than 2°C and salinity greater than 34.8, adapted from Beszczynska-Möller et al., (2012) who only used $T > 2^{\circ}\text{C}$ without salinity constraint. From their study, the mean observed temperature of the AW inflow at Fram Strait over 1997-2010 was $3.1 \pm 0.1^{\circ}\text{C}$. The simulated mean temperature of the AW inflow from our model is about 1°C warmer, $3.85 \pm 0.01^{\circ}\text{C}$ in ANHA12 over 2011-2019 and $4.14 \pm 0.01^{\circ}\text{C}$ in ANHA4 over 2011-

2016 (Table 3.2). The comparisons show that our model tends to simulate a warmer AW, but it might also be due to the warming trend over recent years. We detail the interannual and seasonal variability of the thermohaline structure of the AW in Fram Strait in Figures S1 and S2. The temperature core for the AW is maximum in 2017, reaching 6 °C. This is accompanied by a strong northward flow at a velocity of over 15 cm/s. Concerning the seasonal cycle, the temperature core is cooler in the winter and spring months, typically under 5 °C. It warms in the summer on account of seasonal surface warming. The salinity core does not show any obvious seasonality. Therefore, more buoyant waters can be found above 200 m depth in the summer and fall, indicated by the deeper depth of the isopycnal line $\sigma = 27.9 \text{ kg/m}^3$.

Table 3.2 Long-term means of the AW temperature, oceanic volume and heat transport through Fram Strait and the BSO from ANHA4, ANHA12 and available observations. ANHA4: averaged over 2011-2016; ANHA12: averaged over 2011-2019; a: Mean over 1997-2010 from Beszczynska-Möller et al. (2012); b: Mean over 1997-2006 from Schauer et al. (2008); c: Mean over 1997-2007 from Smedsrud et al. (2010)

Sections		Fram Strait	BSO
AW Definitions		T > 2, S > 34.8	T > 3, S > 34.8
ANHA4	Volume Transport (Sv)	3.2±0.5	2.7±0.3
	Heat Transport (TW)	60.8±3.2	78.3±9.8
ANHA12	Volume Transport (Sv)	2.4±0.4	2.9±0.3
	Heat Transport (TW)	45.6±7.5	86.3±7.0
Observations	Volume Transport (Sv)	3.0±0.2 ^a	3.2 ^c
	Heat Transport (TW)	26-50 ^b	73 ^c

In contrast to Fram Strait, the BSO is a much broader and shallower Arctic gateway. Since there is a higher temperature core of up to 9 °C in the model, we define the AW thresholds as the temperature is greater than 3 °C and the salinity greater than 34.8 for the BSO, consistent with (Oziel et al., 2016). The model successfully captures some fundamental features of the dynamic structure of the water masses, as observed in Ingvaldsen et al., (2004) and Skagseth et al., (2008). Along the Norwegian Coast, the temperature core does not overlap the salinity core, but with the freshest water, which means water containing a great amount of heat could be fresh referenced to salinity of 34.8. This fraction of the warm and fresh water mass is carried by the Norwegian Coastal Current that is not primarily of Atlantic origin. The AW inflow through the BSO is manifest as a wide branch near the central section reaching the deeper part of the BSO and a relatively narrow branch sitting to the south. The mean AW inflow is a barotropic structure as the cores show uniform vertical velocity profiles. Compared to the annual mean velocity in Fram Strait, the mean AW inflow speed crossing the BSO is weak, at less than 10 cm/s. Other than the AW recirculation branches, there is some relatively colder and fresher water of Arctic origin above the ridge flowing out of the Barents Sea (Figure 3.2f).

The mean modelled and observed temperature of the AW inflow in the BSO over the period of 2000-2010 has been estimated as 5.5-6 °C and exhibited a warming trend in that decade (Wang et al., 2019). Our simulated temperature average for the AW inflow is calculated to be slightly warmer, 6.00 ± 0.03 °C in ANHA12 over 2011-2019 and 6.28 ± 0.03 °C in ANHA4 over 2011-2016 (Table 3.2). We present the interannual and seasonal changes in the thermohaline characteristics of the AW inflow at the BSO in Figures S3 and S4. The banded structure of the velocity field is depicted as two visible AW inflow cores, weaker inflows, return flows and Arctic outflows. They consistently appear each year. The temperature core is more pronounced during

2015-2017. The seasonal variability is substantial with higher temperature cores from August to October and fresher salinity cores from November to March on the southern side along the Norwegian coast, as well as stronger AW inflow cores from November to January.

3.3.2 Transports through the Fram Strait and BSO

In order to further elucidate the AW inflow variability through these two gateways, we then quantify the AW volume and heat transport on the interannual and seasonal time scales (Figure 3.3). The volume and heat transport for the AW inflow at Fram Strait are low in 2014 and 2019 (~ 2 Sv and ~ 35 TW) and high in 2017 (~ 2.8 Sv and ~ 55 TW). The correlation coefficient between the volume and heat transport is 0.93, significant at the 99 % level (p -value=0.0003). The peak-to-peak amplitude of the interannual fluctuation of the volume transport is $\sim 30\%$ of the mean volume transport. The long-term means of volume and heat transport from ANHA4 and ANHA12 are comparable to the mooring results of 3.0 ± 0.2 Sv (Beszczynska-Möller et al., 2012) and 26-50 TW (Schauer et al., 2008) (Table 3.2). At the BSO, both volume and heat transport peak in 2015, with the volume transport of ~ 3.4 Sv and the heat transport of ~ 100 TW. The correlation coefficient between the volume and heat transport at the BSO is 0.80, significant at the 99 % level (p -value=0.009). From the modelled studies and available observational results, we find that the long-term mean volume transport of the FSBW and BSBW is of the roughly equivalent intensity, ~ 3 Sv,

but the model BSBW plays a relatively larger role in bringing heat into the Arctic Ocean than the FSBW.

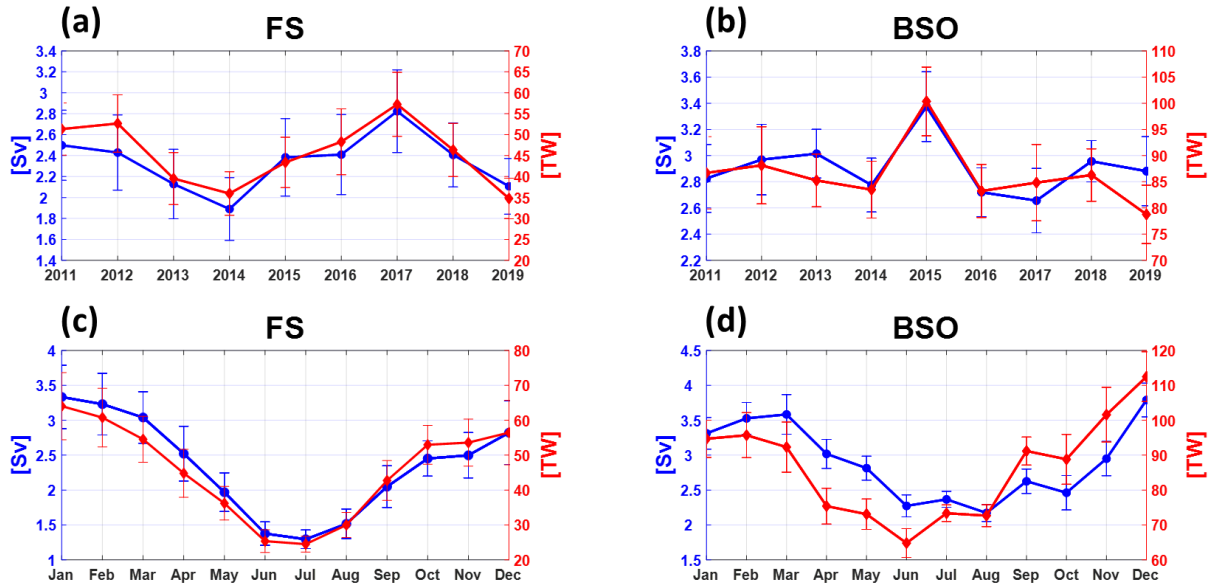


Figure 3.3 Top row: the interannual variability of volume (blue) and heat transport (red) for the Atlantic Water at Fram Strait (a) and the BSO (b) over 2011-2019 with standard error estimates included (standard deviation over the square root of the number of the data samples). Bottom row: Fram Strait (c) and the BSO (d), but for the seasonal variability. The heat transport is referenced to 0 °C. Positive values mean towards the Arctic Ocean, i.e. transports are positive northwards across Fram Strait and eastwards across the BSO.

We illustrate the seasonal cycle of the heat and volume transport at Fram Strait (Figure 3.3c), which is in good agreement with Figure 3.4c from Beszczynska-Möller et al., (2012). The volume and heat transport for the AW inflow at Fram Strait reaches its minimum in July (~1.3 Sv and ~25 TW) and maximum in January (~3.3 Sv and ~64 TW), with substantially higher transport in the winter months (January-March). The fluctuation in oceanic heat transport is strongly correlated to volume

transport. The overall annual mean cycle for the AW inflow through the BSO demonstrates a similar variation pattern of low transport in the summer and high transport in the winter, spanning a range from ~ 2.2 to ~ 3.8 Sv for volume transport and from ~ 65 to ~ 112 TW for heat transport. The summer minima for volume and heat transport at the BSO are not synchronous. The higher AW inflow during fall and winter than summer is largely due to the stronger AW velocity cores in the fall and winter months (Figure S2, S4). This systematic annual cycle is passed down from the upstream transport variability of the eastern branch of the North Atlantic Current in the Norwegian Sea Ingvaldsen et al., (2004) and Orvik et al., (2001), which is induced by the wind pattern variability over the Nordic Seas. The wind forcing pattern is manifested as a strong cyclonic wind stress curl in the winter associated with the Icelandic Low, whose intensity is reflected by a high winter NAO index. Since this distinct seasonal cycle exists in both gateway straits, it is less likely to be on account of their respective local effects.

3.3.3 AW Inflow Pathway from Online Passive Tracers

Online passive tracers representing the FSBW ($T > 2$ °C & $S > 34.8$) and BSBW ($T > 3$ °C & $S > 34.8$) are simulated to depict the propagation of the AW inflow in the pan-Arctic region from 2002 to 2018. We attach a video illustrating the changing state during the simulation time (Video S1). We also show a snapshot of the vertically integrated AW tracer concentration on June 4, 2019 (Figure 3.4). The large-scale circulation of the FSBW features the circumpolar boundary current, marching along the continental slope and basin edges. It arrives at the SAT and distributes over the area through the first year and a half. Continuing along its route, it reaches the Lomonosov Ridge and enters the Canadian Basin after roughly three years of simulation. It first reaches the slope of the Canada Basin in the middle of 2007 and then more tracers accumulate in the Canada Basin. It also gradually accumulates in the interior of the eastern part of the Eurasian Basin and the Makarov

Basin. The vertically integrated tracer concentration is approximately 600 m along the margins of the Arctic Basin, whereas the concentration in the central basin in proximity to the CAA is half of that value. In terms of the BSBW, the tracers enter the Arctic Basin through the eastern side of the SAT after passing through the Barents Sea, or flow along the BSO as return flows and then follow the trajectory of the FSBW. The general spatial patterns of the tracers from the two branches are quite similar but still exhibit some discrepancies. The BSBW tracers have the highest concentration in the eastern Arctic Basin in the vicinity of the Lomonosov Ridge. It has two-thirds of the concentration formed by the FSBW tracers toward the end of the simulation (Figure 3.4). Being constrained by the Chukchi Borderland, the distribution of the BSBW tracers is not significantly high along the slope of the Canada Basin. We notice that the AW tracers are mainly bounded in the Arctic Basin, with only limited loss via Fram Strait and with a smaller portion export via the CAA. Integrating these two branch waters together, the concentration in the eastern Arctic Basin is substantially larger than the other parts of the Arctic Ocean at the end of the integration time (Figure 3.4a), with a tracer concentration of nearly 1100 m.

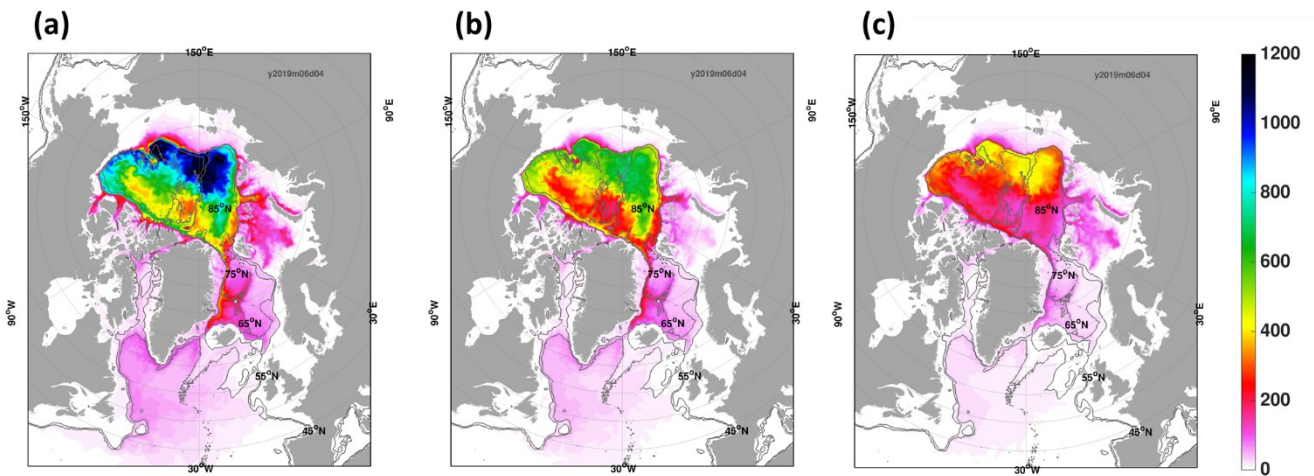


Figure 3.4 A snapshot of the vertically integrated AW tracer concentration on June 4, 2019 (a) particles are released from a combination of Fram Strait and the BSO; (b) from Fram Strait solely; (c) from the BSO solely.

3.3.4 *The Discovery and Sources of the CAW*

We calculate the volume transport for the AW at S3 and S6 based on the definition of $T > 0$ °C and $S > 34.8$ (Figure 3.5), referenced to Dmitrenko et al., (2015) where they defined $T > 0$ °C and $34.75 < S < 34.95$ for the FSBW and $T > 0$ °C and $S > 34.9$ for the “True” mode of the BSBW in the SAT. Other than the peak shown at the beginning of 2017, the most obvious feature in the timeseries of the transport at S3 is the significant transport reductions in 2013 and 2014, indicated by the shading in Figure 3.5a. The reductions last for a few months, although the one in 2014 has a longer duration. The volume transport is below 2 Sv during both events. Farther along the pathway at S6, the AW transports reduce to zero, or even reverse in sign during these events. Exploring these events, we originally considered whether the circulation had temporarily reversed. After further study, we found that instead of reversing, the negative transports were associated with the AW being replaced by a colder water mass that did not satisfy the criteria for the AW we had been using. Given that the replacement water mass keeps its salinity properties but with below-zero temperature, we define this water mass as CAW. The CAW also differs from the regular AW with its higher density. We then compute the volume transport of the CAW, which is defined as -1 °C $< T < 0$ °C, $S > 34.8$ for B2 and -0.5 °C $< T < 0$ °C, $S > 34.8$ for other sections. The pulses of the CAW are clear during 2013 and 2014. The CAW replaces the regular AW and thus causes the reductions in the regular AW transport during the corresponding time periods. The CAW transport increases following its poleward pathway from B2 to S3, and reaches a maximum at S3. The CAW transport at B2 is between 2 and 3 Sv during both events. Increasing by more than twofold from B2, the CAW transport at S3 is 6 Sv in the 2013 event and 7 Sv in 2014. The CAW signal has been greatly amplified in this section. The time lag of one or two months between its upstream sections is expected because of the circulation timescale over a basin-wide area. We do a simple calculation

using velocity $v=20$ cm/s and time $t=45$ days to get a travelling distance of around 750 km, which is the rough distance between S1 and S2. We do not see the CAW anomaly from the sections we set along the FSBW pathway from Fram Strait to SAT (not shown). We notice that only when the CAW flux at B2 (near SAT) has a large enough volume and duration, can it trigger the domino chain effect of the CAW anomaly signals in the downstream sections. The start and end months of the CAW events at each section are listed in Table 3.3.

To identify the structure and distribution of the CAW and to uncover its variations within an annual cycle, we illustrate a cross-trough section temperature plot at B2 and the horizontal region temperature plot near SAT in 2014 when a significant CAW anomaly occurs (Figure S5). The hydrographic pattern of the water masses flowing through the SAT is manifested as warm FSBW entering the SAT with a temperature core of 1-2 °C along the western flank, the cold and denser BSBW at the opposite side of the trough, and the extremely cold and fresh surface ArW in the top 100 m. These water masses interact and vary throughout the year, but a distinct and unstable vertical density front over the water column consistently exists. From March to August, the CAW sits over the slope of the eastern side of B2 with a velocity of over 20 cm/s before sinking to the ocean bottom (Figure S5a and Table 3.3). It is connected to the surface cold water until it is cut off by the reappearance of the regular AW at the upper slope. From October to December, two AW temperature cores are shown in the transect plot, but they have different origins from the FSBW and BSBW respectively (Figure S5a). Only a small amount of the CAW remains at the ocean bottom close to the eastern side. As the CAW occupies the water column at the depth of 200-500 m, by averaging the temperature field over that depth range from the ocean model, we are able to show where the CAW exists at the entrance from the Barents Sea to the Arctic Basin (Figure S5b). The CAW is clearly visible at the southern and eastern sides of the SAT and the Voronin Trough

throughout the CAW anomaly duration. They are combined to drain the CAW from the Barents Sea.

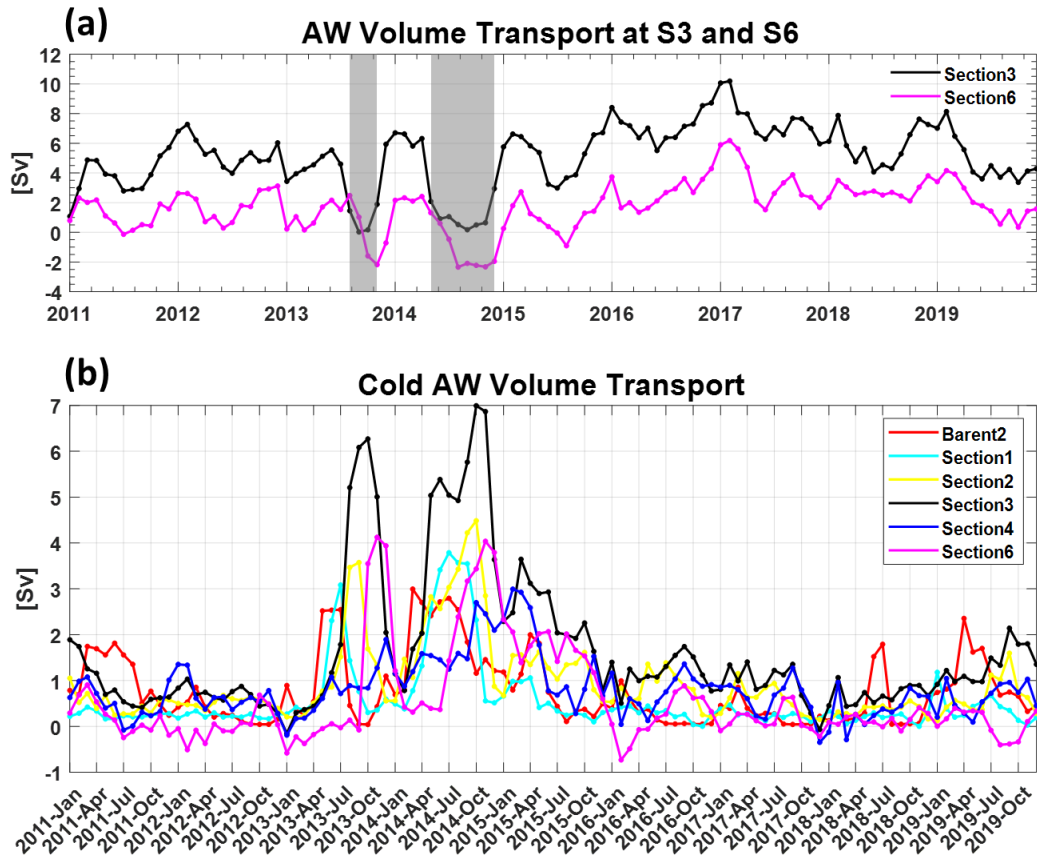


Figure 3.5 (a) Monthly AW volume transport at S3 from 2011-2019; (b) Monthly CAW volume transport at Barent2 (B2), Section1 (S1), Section2 (S2), Section3 (S3), Section4 (S4) and Section6 (S6) from 2011-2019; The locations of each section are shown in Figure 3.1.

Table 3.3 The duration of the apparent CAW signals at some sections in 2013 and 2014. The CAW pulses are apparent when the volume transport is larger than 3 Sv at S3, and it is larger than 2 Sv for the other sections.

Years	2013	2014
B2	May-Jul	Mar-Aug
S1	Jun-Jul	May-Oct

S2	Aug-Sep	Jul-Nov
S3	Aug-Nov	May-Dec
S6	Oct-Dec	Aug-Jan 2015

To probe the source of the CAW, we conduct Ariane experiments for the BSBW and FSBW. Nearly 5000 particles are homogeneously released all at once at the BSO, representing the AW inflow ($T > 3$ °C, $S > 34.8$ and $v > 0$ m/s). Three experiments start in July of 2012, 2015, and 2017 respectively and run forward in time to the end of 2019. For the first experiment, we plot a snapshot of the temperature of all the particles after two years (Figure 3.6b). At the end of the first year, the particles cover the whole Barents Sea and begin to enter the Eurasian Basin through SAT. After two years, the distribution of the particles demonstrates a bifurcation near Lomonosov Ridge. The particles get cooled along their poleward pathway, from $5+$ °C at the BSO to $0-$ °C near Lomonosov Ridge. The first experiment starting in July 2012 has undergone the conditions that trigger the CAW production when the particles were passing through the Barents Sea in 2013 and 2014. In this Ariane experiment, the particles with $T < 0$ °C at the AW layer (400-1200 m deep) form a clear trajectory along the rim of the eastern Eurasian Basin. Instead, few dispersed particles along the trajectory are seen in the other two experiments where the particles are seeded from July 2015 and 2017 (Figure S6b & d). These results using Ariane tracers verify the existence of the CAW events in the ocean model during 2013 and 2014.

We similarly release the particles at Fram Strait, representing the FSBW ($T > 2$ °C, $S > 34.8$ and $v > 0$ m/s). We notice that a trajectory formed by the cold particles appears again but only in the first experiment where particles are released from July 2012 (Figure S7). Considering that no CAW signal appears in the FSBW before reaching the SAT, we suggest that the FSBW also contributes to the CAW anomaly but in a slightly different way. After flowing along the continental slope, the particles enter the SAT, mix with the BSBW, and get cooled into the CAW. Here we point out that

even though we have doubled the number of seeding particles, the trajectory is not as clear as the one shown in Figure 3.6c, which implies that the primary source of the CAW comes from the BSBW rather than the FSBW.

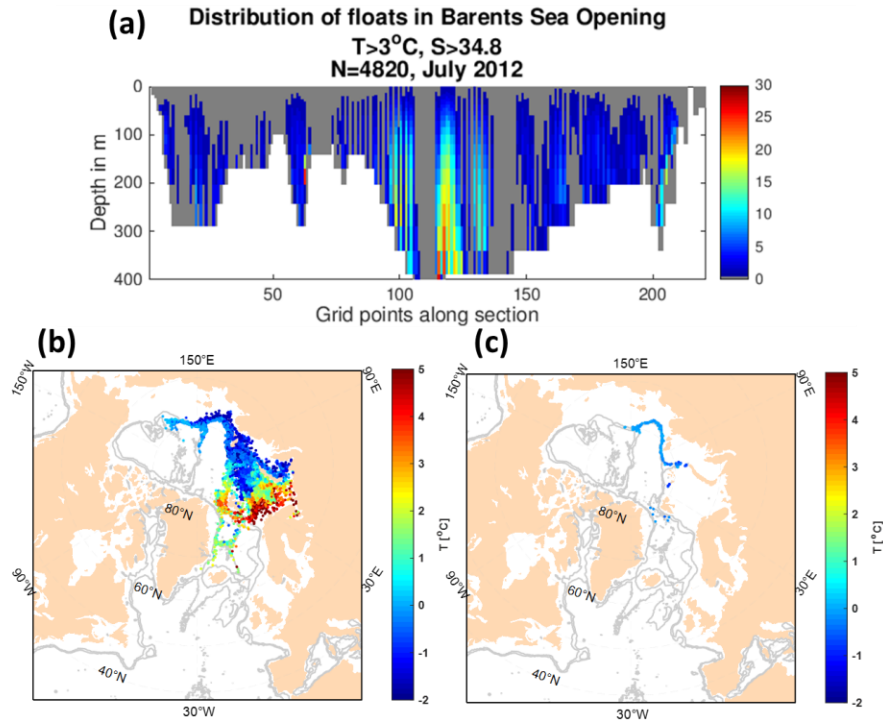


Figure 3.6 (a) Distribution of particles in the BSO seeded in July 2012. (b) Distribution of all the particles after a two-year forward simulation scheme, that is, a snapshot in July 2014, (c) Only exhibiting the particles with a temperature below 0°C at the AW layer (between 400-1200 m deep) from (b).

3.3.5 Physical mechanisms for the CAW Formation

We now investigate the physical mechanisms causing the CAW production. As the CAW is mainly from the BSBW, the Barents Sea is a breeding ground for the CAW, where the air-ocean coupling heat flux is especially intense (Smedsrud et al., 2013). We simulate the annual mean transformation rate for the CAW in response to surface heat and freshwater fluxes from 2011 to 2019. Taking the

year of 2013 for example, when the first CAW event occurs, we first show the transformation rate for the CAW as a function of the surface density (Figure 3.7a). The positive values represent the removal of buoyancy, which means the water has been densified, hence more CAW is formed. The transformation to the CAW is typically at the isopycnal range of $27.9\text{-}28.3\text{ kg/m}^3$. The heat flux is dominant for the transformation to the denser water mass, whereas the freshwater flux acts to suppress the transformation and has a comparatively little impact. This finding is consistent with Myers & Donnelly, (2008). They found that it is the surface heat flux (primarily sensible heat flux component) that determines the transformation rate of the LSW.

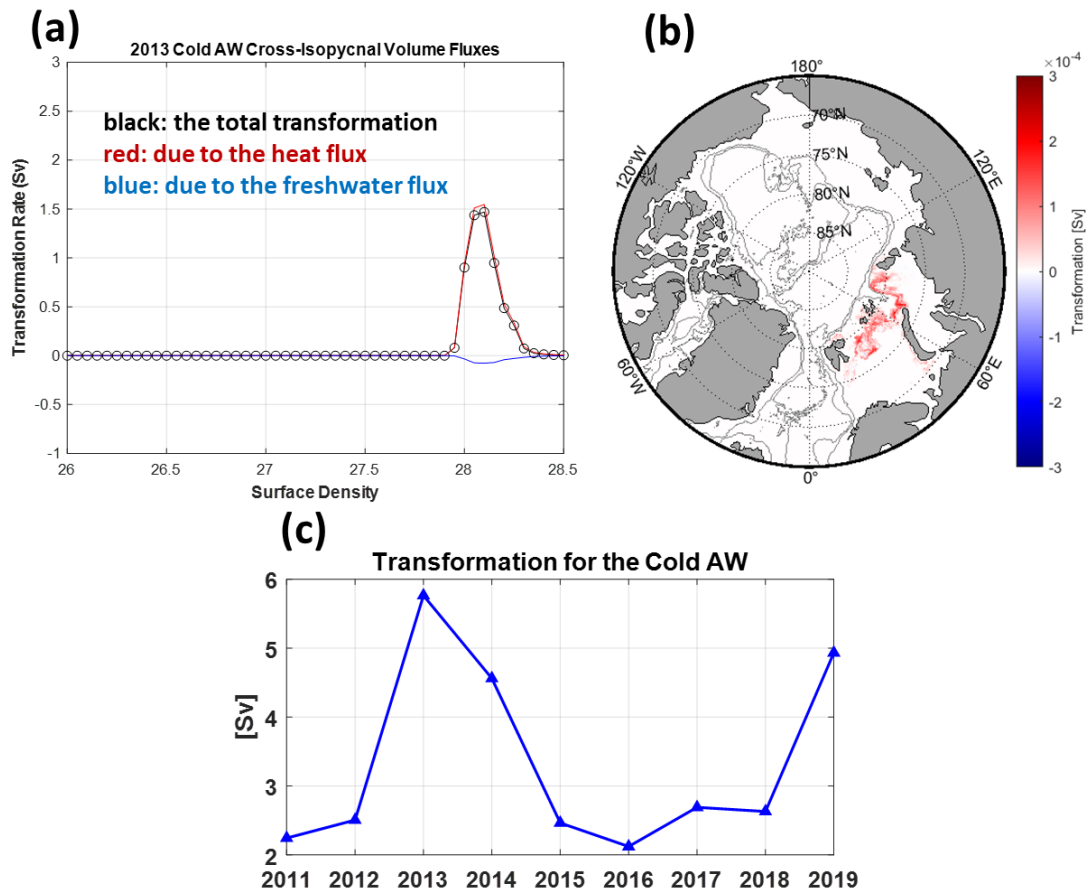


Figure 3.7 (a) The CAW cross-isopycnal volume fluxes (Sv) changing with the surface density anomaly (kg/m^3) in 2013. The red and blue lines exhibit the transformation rate due to heat and

freshwater fluxes, respectively. The black line is the sum of both. (b) the spatial pattern of the transformation rate at $\sigma^*=28.1 \text{ kg/m}^3$ and $\Delta\sigma=0.05 \text{ kg/m}^3$. (c) the interannual variability of the transformation rate for the CAW from 2011 to 2019.

The map in Figure 3.7b demonstrates the spatial pattern of the transformation at a particular density bin in 2013. It exemplifies that the transformation predominantly occurs in the Barents Sea, especially along the southern and eastern sides of the SAT and in the Voronin Trough where we also can see the CAW (Figure S5). The mean surface heat loss is $\sim 90 \text{ W/m}^2$ and the E-P is $\sim 16 \text{ cm/yr}$ for these regions where the transformation into the CAW is most pronounced. Integrating the transformation volume for the CAW in the Barents Sea, we can examine the interannual variability of the transformation from 2011 to 2019. The time series Figure 3.7c presents high transformation rates in two consecutive years, $\sim 5.8 \text{ Sv}$ in 2013 and $\sim 4.5 \text{ Sv}$ in 2014. The results are consistent with the pulses of the CAW formation (Figure 3.5, Table 3.3). Therefore, the surface heat flux over 2013-2014 at the Barents Sea provides critical preconditioning for the transformation of the AW into the CAW.

3.3.6 The Evolution and Fate of the CAW

Having explored the origin of the CAW and the processes for its formation, we then investigate the downstream fate of the CAW in the Arctic Basin. We set up another Ariane experiment by releasing around 2000 particles all at once at B2, starting from July 2013. These particles represent the CAW ($-1 \text{ }^\circ\text{C} < T < 0 \text{ }^\circ\text{C}$, $S > 34.8$) entering the Arctic Basin through the SAT. As we have seen in Figure S5a, the particles sit at the slope of the eastern SAT (Figure 3.8a). We present the early stages of the evolution after 15 days, 30 days and 50 days of their release (Figure 3.8b). Only the particles located deeper than 400 m are shown here to avoid too much clutter. Fifteen days after

the particles are seeded, the particles still gather together in close proximity at the tongue of the Voronin Trough, lying at the depth range of 400-600 m. After another 15 days have passed, being colder and saltier than the ambient water, the particles start to move deeper downslope while transiting along their poleward pathway. Fifty days from their release, the particles clearly demonstrate the cascading process that the CAW undergoes, with some distributed near the basin edge of 500 m and successively extending along the 2000 m isobath. At the end of the simulation, the particles entering the Canadian Basin generally reside within the deep layers (>1200 m), whereas the particles staying in the Eurasian Basin spread over the entire depth profile (Figure 3.8c). Furthermore, the particles in the upper layer (<600 m) tend to reside in the eastern Eurasian Basin while the deep ones settle in the interior of the basin near the side of Lomonosov Ridge.

To further evaluate the impact the CAW anomaly has on the Arctic Basin, we calculate the heat and freshwater content integrated over the whole water column from 2011 to 2019 (Figure 3.9). We focus on the eastern region covering the CAW trajectory. We also note that the vertically integrated tracer thickness is exceedingly high within the region from our online passive tracer study (Videos S1). The heat content experienced a significant downturn right after the CAW events in 2013 and 2014. It reaches the minimum in 2015 and then returns to the previous level. The heat content has reduced by over 50% by 2015 compared to 2013. The decline is dictated by the CAW anomaly signals propagating to the region. The heat content quantifies the heat contained in the AW layer referenced to 0 °C. The CAW events have a negligible impact on the interannual variability of the freshwater content (Figure 3.9b). The signals have been masked by the strong seasonality that is associated with the sea ice melt and freeze. In contrast to the freshwater content time series, the heat content time series indicates that seasonality has a much weaker influence.

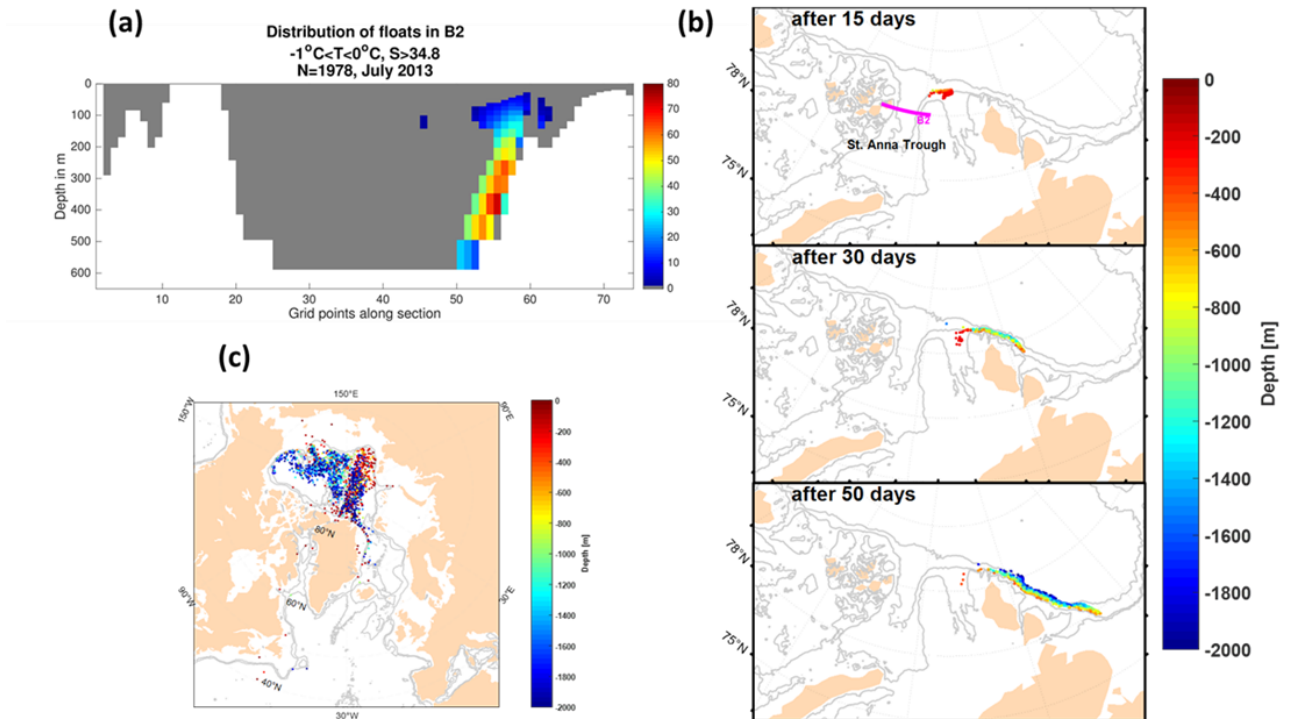
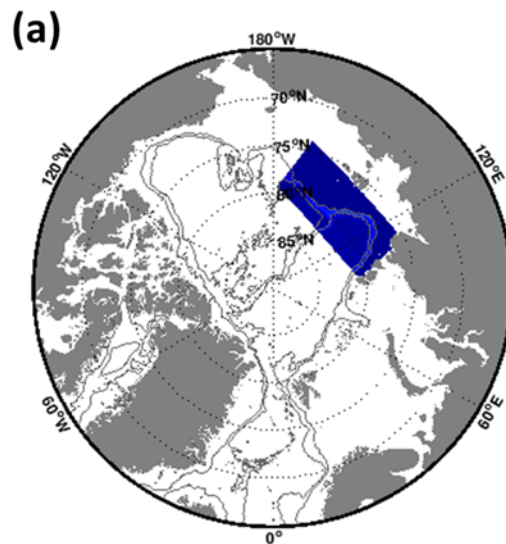


Figure 3.8 (a) Distribution of particles in B2 seeded in July 2013. (b) The locations of the particles after evolving for 15 days, 30 days, and 50 days. (c) The locations of the particles at the end of the simulation, on December 31, 2019.



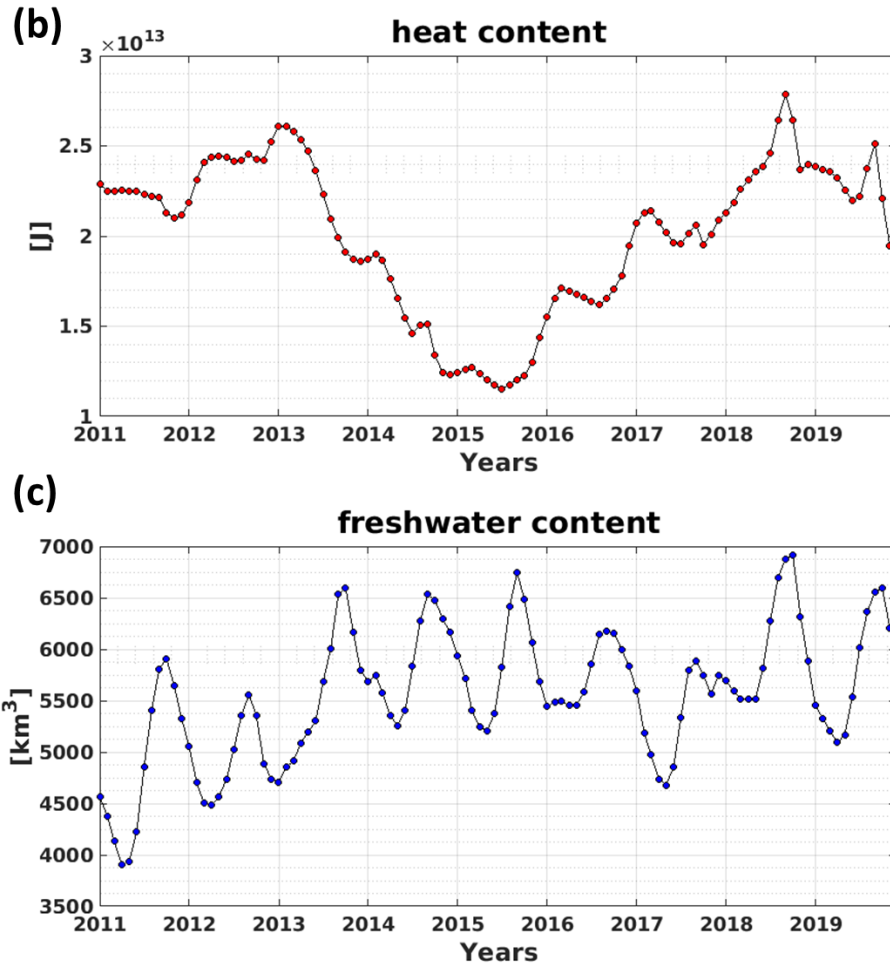


Figure 3.9 (a) The simulated region in the Arctic Basin, indicated in blue quasi-parallelogram. (b) the heat content and (c) the freshwater content integrated from the whole water column from 2011 to 2019.

3.4 Summary and Discussion

In this paper, we model the AW in the Arctic Ocean based on its distinct thermohaline properties at two key Arctic gateways – Fram Strait and the BSO. The AW both at Fram Strait and the BSO present clear inflow cores with a more barotropic constituent than the downstream sections (Pnyushkov et al., 2015). The interannual variability of the AW inflow transport at Fram Strait and the BSO exhibits different patterns but the seasonal cycles are more similar. During the fall and

winter months, the intensified AW inflow flowing at a faster speed facilitates the volume and heat transport through these two sections. The model results from ANHA4 and ANHA12 demonstrate general agreement with the observations regarding long-term means of the volume and heat transport at Fram Strait and the BSO, indicating that we can use the ocean model simulations to study questions of AW propagation in the Arctic Ocean. In comparison to the FSBW, we find that the BSBW is more conducive to transporting heat to the Arctic Ocean across the entrances. The pathways of the FSBW and BSBW in the Arctic Ocean are depicted using online passive tracers. The tracers concentrate in the eastern Arctic Basin in the proximity of the Lomonosov Ridge. The amount of flux entering the Canada Basin is limited as the tracers are blocked by the Chukchi Borderland (Video 1).

By looking at the transport reductions of the AW at S3 and the transport anomalies of the AW at S6 in 2013 and 2014, we detect the CAW pulses along the rim of the eastern Eurasian Basin. Our results show that the cold dense AW is cascading off the shelf from the eastern flank of the SAT and the Voronin Trough. Studies from Luneva et al., (2020) also show that St. Anna Trough is one of the most favourable sites that produce intense dense water descending fluxes. The CAW signals have been markedly amplified when reaching S3 (Figure 3.5). We speculate that this is due to the considerable mixing/entrainment with the ambient AW along the path to S3, which leads to more surrounding AW transforming to the CAW. The region above the continental slope along the pathway is a mixing hotspot (Schulz et al., 2021). The diapycnal mixing owing to the temperature gradient between the two water masses results in the largest portion of the heat loss of the AW. Our Ariane tracer forward analysis suggests that the source of the CAW is primarily from the BSBW, and with minor contributions from the FSBW. The FSBW contributes to the CAW production by mixing with the BSBW at the eastern SAT. The transformation into the CAW

principally occurs in the Barents Sea, and we find that the vigorous and enduring sea surface cooling over 2013-2014 in the Barents Sea provides critical preconditioning for the transformation from the AW to the CAW. Additionally, the warm and saline AW inflows through Fram Strait and the BSO are not high during these two years, which limits heat input to the Barents Sea.

The CAW is not uncommon near the SAT, which we also see from the observational arrays in earlier years, e.g. September 2009 (Dmitrenko et al., 2015; Zhurbas & Kuzmina, 2020). As our analysis suggest, our models are inclined to simulate warmer water than the observations (Table 3.1), but this cannot alter the perspective that an increasing amount of the colder and denser AW could be produced during 2013-2014. Due to the restricted short simulation period from our study, we could not diagnose the trend of more warm and saline AW flowing into the Arctic Ocean through Fram Strait and the BSO, which acts as a crucial attribute to the Arctic Atlantification (Polyakov et al., 2017). However, the high variability in the AW inflows we have presented in this research can partly account for the AW fluctuations at the AW layer of the Arctic Basin with abrupt cooling/warming events.

The heat transport through the BSO is the prime heat source to the Barents Sea and shows an anticorrelation with the winter Barents Sea ice extent (Årthun et al., 2012; Docquier et al., 2020). As sea ice functions like an insulating layer, the winter sea ice retreat as a result of the Arctic Atlantification makes the Barents Sea more susceptible to atmospheric forcings, which thus enhances the air-sea heat fluxes (Moore et al., 2022). This scheme thereby increases the possibility to create appropriate conditions for the CAW formation, which is dependent on the effective region for cooling and less heat transport advected to the area. Farther downstream along the AW progression pathway, the sea ice extent decline also promotes stronger upper-ocean currents and associated vertical shear, coinciding with the enhanced ventilation of the AW and the weakening

of stratification in the Eastern Arctic Ocean (Polyakov et al., 2020). All in all, the AW into the Arctic Basin could be cold ($T < 0$ °C). The CAW has significantly reduced the heat content of the eastern Arctic Basin in 2015 according to our study, and it also has a potential impact on the structure of the nutricline and the biological production along the circulation pathways (Jung et al., 2021; Polyakov et al., 2020). However, more future studies are needed to garner a better understanding of its ramifications to the Arctic Ocean under the context of global warming.

Acknowledgments

We gratefully acknowledge the financial and logistic support of grants from the Natural Sciences and Engineering Research Council (NSERC) of Canada. These include a Discovery Grant (rgpin227438-09) awarded to P.G. Myers, and a Climate Change and Atmospheric Research Grant (VITALS - RGPCC 433898). We are grateful to the NEMO development team and the Drakkar project for providing the model and continuous guidance. We would also like to thank G. Smith for the model atmospheric forcing fields, made available by Environment and Climate Change Canada (http://weather.gc.ca/grib/grib2_glb_25km_e.html). We thank Westgrid and Compute Canada for computational resources, where all model experiments were performed. The model code based on the NEMO model is available at <https://www.nemo-ocean.eu/> (last access: 28 May 2017, Madec, 2008). Details on the ANHA configuration used are available at <http://knossos.eas.ualberta.ca/anha/index.php> (last access: 8 September 2017), with files for the experiment used in this paper at <https://doi.org/10.7939/DVN/GIXGXB> (Hu, 2020).

4. Conclusions

The encroachment of the warm and saline Atlantic Water has a large and broad impact on the Arctic Ocean. The AW stems from the Atlantic Ocean, with distinct thermohaline properties. The warm and saline constituent is delivered by the AMOC from the tropics to the high latitude regions. The AW inflow experiences a substantial change as it enters the Nordic Seas where it undergoes the winter-time atmospheric cooling and mixes with the fresher water near the marginal ice zone. The Nordic Seas exhibited a warming and salinification trend in recent decades. The AW flows into the Arctic Ocean through Fram Strait and the BSO and forms the AW boundary current along the slope of the Arctic Basin. Based on the distinguishing characteristic of the AW properties, we have used temperature and salinity thresholds as dynamical tracers to define the water mass. By the implementation of the online passive tracers and ARIANE particles in ANHA4 and ANHA12 experiments, we are able to evaluate the variability of the AW at Fram Strait and the BSO, track the pathway of the AW inflows, and investigate how it transforms and evolves along its poleward pathway.

In the seasonal cycle, the AW inflow through Fram Strait and the BSO is the comparatively higher during fall and winter. This annual cycle is inherited from the eastern AW branches in the Nordic Seas, which is governed by a strong winter cyclone linked to the Icelandic Low. Meanwhile, the interannual variability of the AW inflow through these two Arctic gateways is not synchronous. A peak appears in 2015 for the BSBW while it is two years after that for the FSBW. On the long-term mean transport calculation, the BSBW brings more heat into the Arctic Ocean via its gateway in comparison with the FSBW, even though their AW volume transport has little difference. In addition to facilitating sea ice retreat, the heat transported to the Barents Sea is mostly lost due to

the air-sea interaction over the shallow continental shelf. The surface heat flux in the Barents Sea leads to the transformation of the AW. By the time it reaches near St. Anna Trough, the warm AW has been cooled to be only slightly above 0 °C.

While exploring the transformation of the AW, a cold mode of Atlantic Water (CAW) with a temperature below 0 °C that significantly reduced the heat content of the eastern Arctic, is identified. We discovered two strong CAW anomaly events along the rim of the eastern Eurasian Basin during 2013 and 2014, with a tendency to amplify en route until section S3. The CAW is a water mass that keeps its saline property but with below-zero temperature, so it differs from the regular AW with its higher density. This finding has overturned our understanding that the AW is always warm and saline. The dominant contributor to the CAW formation is the intense sea surface cooling at the Barents Sea for two consecutive years. By releasing particles at the Barents Sea Opening and Fram Strait using the offline Lagrangian particle-tracking product Ariane, we found that the source of the CAW is primarily from the BSBW, and it also has secondary contributions from the FSBW. This approach highlights the propagation of the AW through oceanic advection. The CAW signals progress along the typical AW poleward pathway, experience significant mixing with the surrounding waters, and eventually result in a heat content reduction in the AW layer of the eastern Arctic Basin.

Other than the intense air-sea interaction in the Barents Seas, the cause of the CAW is hypothesized to be connected to the hydrographic state further upstream at the Arctic gateways, the Nordic Seas, and eventually linked to the AMOC in the North Atlantic. Our study has verified that the heat transport carried by the AW at the Arctic gateways is relatively low during the years when we have the CAW signals. We could extend our study to the upstream sections that separate the Nordic Seas and the North Atlantic and monitor the interannual variability of the AW volume and heat transport.

For instance, we could look at the characteristic, spatial structure, and variability of the AW inflows through Denmark Strait, Iceland Faroe Ridge, and Faroe-Shetland Channel (DS-IFR-FSC), see how the heat and volume transport compare with the observations and estimates from various model studies, and find out the physical mechanisms dictating their respective heat distributions and contributions to the Nordic Seas. In addition, to depict the AW pathways in the Nordic Seas, it will be interesting to utilize Ariane to study how the AW tracers evolve if they are released at these sections. A quantitative study could be carried out, such as investigating how many tracers will stay in the Nordic Seas, and how many of them will exit through Fram Strait and the BSO. To explore the impact the warm and saline AW has on the Nordic Seas, it will also be worth investigating the heat and salt content change in the Nordic Seas on the interannual and seasonal time scales over the recent years and diagnosing the reported trend using our model.

This study has been conducted to enhance our understanding of the role of the AW in high latitude regions and has built a knowledge base on its circulation and transport pathway in the Arctic Ocean. This study further clarifies the thermodynamic state change of the AW and the spatio-temporal variation along its poleward pathway in the model. The model study is able to provide insight into the potential impacts of global warming on the AW and allow us to make inferences about its evolution in the Arctic Ocean. However, there remains little doubt that we will need a more careful evaluation of the AW in the future. By doing so, we could gain better predictability of its transformation, and its profound impacts on Arctic sea ice, Arctic heat storage, Arctic ecosystems etc.

Bibliography

- Årthun, M., Eldevik, T., Smedsrud, L. H., Skagseth, & Ingvaldsen, R. B. (2012). Quantifying the influence of atlantic heat on barents sea ice variability and retreat. *Journal of Climate*, 25(13), 4736–4743. <https://doi.org/10.1175/JCLI-D-11-00466.1>
- Athanase, M., Provost, C., Artana, C., Pérez-Hernández, M. D., Sennéchaël, N., Bertosio, C., Garric, G., Lellouche, J., & Prandi, P. (2020). Changes in Atlantic Water circulation patterns and volume transports North of Svalbard over the last 12 years (2008-2020). *Journal of Geophysical Research: Oceans*. <https://doi.org/10.1029/2020jc016825>
- Bamber, J., Van den Broeke, M., Ettema, J., Lenaerts, J., & Rignot, E. (2012). Recent large increases in freshwater fluxes from Greenland into the North Atlantic. *Geophysical Research Letters*, 39, L19501. <https://doi.org/10.1029/2012gl052552>
- Bernard, B., Madec, G., Penduff, T., Molines, J.-M., Treguier, A.-M., Le Sommer, J., Beckmann, A., Biastoch, A., Böning, C., Dengg, J., Derval, C., Durand, E., Gulev, S., Remy, E., Talandier, C., Theetten, S., Maltrud, M., Mcclean, J., & De Cuevas, B. (2006). *Impact of partial steps and momentum advection schemes in a global ocean circulation model at eddy-permitting resolution*. 56(5–6), 543–567. <https://doi.org/10.1007/s10236-006-0082-1>
- Beszczynska-mo, A. (2012). *Variability in Atlantic water temperature and transport at the entrance to the Arctic Ocean, 1997–2010*. 69, 852–863.
- Blanke, B. (2002). *A Lagrangian numerical investigation of the origins and fates of the salinity maximum water in the Atlantic*. 107(C10). <https://doi.org/10.1029/2002jc001318>
- Bower, A., Lozier, S., Biastoch, A., Drouin, K., Foukal, N., Furey, H., Lankhorst, M., Rühls, S., & Zou, S. (2019). Lagrangian Views of the Pathways of the Atlantic Meridional Overturning Circulation. *Journal of Geophysical Research: Oceans*, 124(8), 5313–5335.

<https://doi.org/10.1029/2019jc015014>

- Buckley, M. W., & Marshall, J. (2016). Observations, inferences, and mechanisms of the Atlantic Meridional Overturning Circulation: A review. *Reviews of Geophysics*, 54(1), 5–63. <https://doi.org/10.1002/2015RG000493>
- Carmack, E. C. (2007). The alpha/beta ocean distinction: A perspective on freshwater fluxes, convection, nutrients and productivity in high-latitude seas. *Deep Sea Research Part II: Topical Studies in Oceanography*, 54(23–26), 2578–2598. <https://doi.org/10.1016/j.dsr2.2007.08.018>
- Cavalieri, D. J., & Parkinson, C. L. (2012). Arctic sea ice variability and trends, 1979-2010. *Cryosphere*, 6(4), 881–889. <https://doi.org/10.5194/tc-6-881-2012>
- Chafik, L., Nilsson, J., Skagseth, Ø., & Lundberg, P. (2015). *On the flow of Atlantic water and temperature anomalies in the Nordic Seas toward the Arctic Ocean*. 120(12), 7897–7918. <https://doi.org/10.1002/2015jc011012>
- Chanut, J., Barnier, B., Large, W., Debreu, L., Penduff, T., Molines, J. M., & Mathiot, P. (2008). Mesoscale Eddies in the Labrador Sea and Their Contribution to Convection and Restratification. *Journal of Physical Oceanography*, 38(8), 1617–1643. <https://doi.org/10.1175/2008jpo3485.1>
- Comiso, J. C. (2012). Large decadal decline of the arctic multiyear ice cover. *Journal of Climate*, 25(4), 1176–1193. <https://doi.org/10.1175/JCLI-D-11-00113.1>
- Comiso, J. C., Meier, W. N., & Gersten, R. (2017). Variability and trends in the Arctic Sea ice cover: Results from different techniques. *Journal of Geophysical Research: Oceans*, 122(8), 6883–6900. <https://doi.org/10.1002/2017JC012768>
- Crews, L., Sundfjord, A., & Hattermann, T. (2019). How the Yermak Pass Branch Regulates

- Atlantic Water Inflow to the Arctic Ocean. *Journal of Geophysical Research: Oceans*, 124(1), 267–280. <https://doi.org/10.1029/2018jc014476>
- Dai, A., Qian, T., Trenberth, K. E., & Milliman, J. D. (2009). Changes in Continental Freshwater Discharge from 1948 to 2004. *Journal of Climate*, 22(10), 2773–2792. <https://doi.org/10.1175/2008jcli2592.1>
- Dai, A., & Trenberth, K. E. (2002). Estimates of Freshwater Discharge from Continents: Latitudinal and Seasonal Variations. *Journal of Hydrometeorology*, 3(6), 660–687. [https://doi.org/10.1175/1525-7541\(2002\)003<0660:eofdfc>2.0.co;2](https://doi.org/10.1175/1525-7541(2002)003<0660:eofdfc>2.0.co;2)
- Dmitrenko, I. A., Rudels, B., Kirillov, S. A., Aksenov, Y. O., Lien, V. S., Ivanov, V. V, Schauer, U., Polyakov, I. V, Coward, A., & Barber, D. G. (2015). Atlantic water flow into the Arctic Ocean through the St. Anna Trough in the northern Kara Sea. *Journal of Geophysical Research: Oceans*, 120(7), 5158–5178. <https://doi.org/10.1002/2015jc010804>
- Docquier, D., Fuentes-franco, R., Koenig, T., & Fichefet, T. (2020). *Sea Ice — Ocean Interactions in the Barents Sea Modeled at Different Resolutions*. 8(May), 1–21. <https://doi.org/10.3389/feart.2020.00172>
- Dukhovskoy, D. S., Myers, P. G., Platov, G., Timmermans, M.-L., Curry, B., Proshutinsky, A., Bamber, J. L., Chassignet, E., Hu, X., Lee, C. M., & Somavilla, R. (2015). *Greenland freshwater pathways in the sub-Arctic Seas from model experiments with passive tracers*. n/a-n/a. <https://doi.org/10.1002/2015jc011290>
- Fichefet, T., & Maqueda, M. A. M. (1997). *Sensitivity of a global sea ice model to the treatment of ice thermodynamics and dynamics*. 102(C6), 12609–12646. <https://doi.org/10.1029/97jc00480>
- Fratantoni, P. S., & Pickart, R. S. (2007). *The Western North Atlantic Shelfbreak Current System*

in Summer. 37(10), 2509–2533. <https://doi.org/10.1175/jpo3123.1>

Frierson, D. M. W., Hwang, Y. T., Fučkar, N. S., Seager, R., Kang, S. M., Donohoe, A., Maroon, E. A., Liu, X., & Battisti, D. S. (2013). Contribution of ocean overturning circulation to tropical rainfall peak in the Northern Hemisphere. *Nature Geoscience*, 6(11), 940–944. <https://doi.org/10.1038/ngeo1987>

Guarino, M.-V., Sime, L. C., Schröder, D., Malmierca-Vallet, I., Rosenblum, E., Ringer, M., Ridley, J., Feltham, D., Bitz, C., Steig, E. J., Wolff, E., Stroeve, J., & Sellar, A. (2020). Sea-ice-free Arctic during the Last Interglacial supports fast future loss. *Nature Climate Change*, 10(10), 928–932. <https://doi.org/10.1038/s41558-020-0865-2>

Haine, T., Böning, C., Brandt, P., Fischer, J., Funk, A., Kieke, D., Kvaleberg, E., Rhein, M., & Visbeck, M. (2008). North Atlantic Deep Water transformation in the Labrador Sea, recirculation through the subpolar gyre, and discharge to the subtropics. In *Arctic-Subarctic Ocean Fluxes: Defining the Role of the Northern Seas in Climate*. https://doi.org/10.1007/978-1-4020-6774-7_28

Hattermann, T., Isachsen, P. E., Appen, W., Albretsen, J., & Sundfjord, A. (2016). *Eddy-driven recirculation of Atlantic Water in Fram Strait*. 1–9. <https://doi.org/10.1002/2016GL068323>.Received

Holliday, N. P., Bacon, S., Cunningham, S. A., Gary, S. F., Karstensen, J., King, B. A., Li, F., & Mcdonagh, E. L. (2018). Subpolar North Atlantic Overturning and Gyre-Scale Circulation in the Summers of 2014 and 2016. *Journal of Geophysical Research: Oceans*, 123(7), 4538–4559. <https://doi.org/10.1029/2018jc013841>

Howell, S. E. L., Derksen, C., Pizzolato, L., & Brady, M. (2015). *Multiyear ice replenishment in the Canadian Arctic Archipelago: 1997-2013*. 120(3), 1623–1637.

<https://doi.org/10.1002/2015jc010696>

Hu, X., Myers, P. G., & Lu, Y. (2019). Pacific Water Pathway in the Arctic Ocean and Beaufort Gyre in Two Simulations With Different Horizontal Resolutions. *Journal of Geophysical Research: Oceans*. <https://doi.org/10.1029/2019jc015111>

Hunke, E. C., & Dukowicz, J. K. (1997). An Elastic–Viscous–Plastic Model for Sea Ice Dynamics. 27(9), 1849–1867. [https://doi.org/10.1175/1520-0485\(1997\)027<1849:aevpmf>2.0.co;2](https://doi.org/10.1175/1520-0485(1997)027<1849:aevpmf>2.0.co;2)

Ingvaldsen, R. B., Asplin, L., & Loeng, H. (2004). Velocity field of the western entrance to the Barents Sea. *Journal of Geophysical Research: Oceans*, 109(3). <https://doi.org/10.1029/2003jc001811>

Isachsen, P E, Koszalka, I., & Lacasce, J. H. (2012). Observed and modeled surface eddy heat fluxes in the eastern Nordic Seas. *Journal of Geophysical Research: Oceans*, 117(C8), n/a–n/a. <https://doi.org/10.1029/2012jc007935>

Isachsen, Pål E, Sørli, S. R., Mauritzen, C., Lydersen, C., Dodd, P., & Kovacs, K. M. (2014). Upper-ocean hydrography of the Nordic Seas during the International Polar Year (2007–2008) as observed by instrumented seals and Argo floats. *Deep Sea Research Part I: Oceanographic Research Papers*, 93, 41–59. <https://doi.org/10.1016/j.dsr.2014.06.012>

Jung, J., Cho, K. H., Park, T., Yoshizawa, E., Lee, Y., Yang, E. J., Gal, J. K., Ha, S. Y., Kim, S., Kang, S. H., & Grebmeier, J. M. (2021). Atlantic-Origin Cold Saline Water Intrusion and Shoaling of the Nutricline in the Pacific Arctic. *Geophysical Research Letters*, 48(6). <https://doi.org/10.1029/2020GL090907>

Kawasaki, T., & Hasumi, H. (2016). The inflow of Atlantic water at the Fram Strait and its interannual variability. *Journal of Geophysical Research: Oceans*, 121(1), 502–519.

<https://doi.org/10.1002/2015jc011375>

Kelly, S., Popova, E., Aksenov, Y., Marsh, R., & Yool, A. (2018). Lagrangian Modeling of Arctic Ocean Circulation Pathways: Impact of Advection on Spread of Pollutants. *Journal of Geophysical Research: Oceans*, 123(4), 2882–2902.

<https://doi.org/10.1002/2017jc013460>

Kuhlbrodt, T., Griesel, A., Montoya, M., Levermann, A., Hofmann, M., & Rahmstorf, S. (2007). On the driving processes of the Atlantic meridional overturning circulation. *Reviews of Geophysics*, 45(2). <https://doi.org/10.1029/2004RG000166>

Large, W. G., & Yeager, S. G. (2009). The global climatology of an interannually varying air - Sea flux data set. *Climate Dynamics*, 33(2–3), 341–364. <https://doi.org/10.1007/s00382-008-0441-3>

Li, J., Pickart, R. S., Lin, P., Bahr, F., Arrigo, K. R., Juranek, L., & Yang, X. (2020). The Atlantic Water Boundary Current in the Chukchi Borderland and Southern Canada Basin. *Journal of Geophysical Research: Oceans*, 125(8). <https://doi.org/10.1029/2020jc016197>

Lozier, M. S., Li, F., Bacon, S., Bahr, F., Bower, A. S., Cunningham, S. A., De Jong, M. F., De Steur, L., Deyoung, B., Fischer, J., Gary, S. F., Greenan, B. J. W., Holliday, N. P., Houk, A., Houpert, L., Inall, M. E., Johns, W. E., Johnson, H. L., Johnson, C., ... Zhao, J. (2019). A sea change in our view of overturning in the subpolar North Atlantic. *Science*, 363(6426), 516–521. <https://doi.org/10.1126/science.aau6592>

Luneva, M. V., Ivanov, V. V., Tuzov, F., Aksenov, Y., Harle, J. D., Kelly, S., & Holt, J. T. (2020). Hotspots of Dense Water Cascading in the Arctic Ocean: Implications for the Pacific Water Pathways. *Journal of Geophysical Research: Oceans*, 125(10). <https://doi.org/10.1029/2020jc016044>

- Madec, G. (2016). *NEMO ocean engine*. 27.
- Marshall, J., Dobson, F., Moore, K., Rhines, P., Visbeck, M., D'Asaro, E., Bumke, K., Chang, S., Davis, R., Fischer, K., Garwood, R., Guest, P., Harcourt, R., Herbaut, C., Holt, T., Lazier, J., Legg, S., McWilliams, J., Pickart, R., ... Smethie, W. (1998). The Labrador Sea Deep Convection Experiment. *Bulletin of the American Meteorological Society*, 79(10), 2033–2058. [https://doi.org/10.1175/1520-0477\(1998\)079<2033:tldsce>2.0.co;2](https://doi.org/10.1175/1520-0477(1998)079<2033:tldsce>2.0.co;2)
- Masina, S., Storto, A., Ferry, N., Valdivieso, M., Haines, K., Balmaseda, M., Zuo, H., Drevillon, M., & Parent, L. (2017). An ensemble of eddy-permitting global ocean reanalyses from the MyOcean project. *Climate Dynamics*, 49(3), 813–841. <https://doi.org/10.1007/s00382-015-2728-5>
- Matsumoto, K. (2017). Tantalizing evidence for the glacial North Atlantic bottom water. *Proceedings of the National Academy of Sciences*, 114(11), 2794–2796. <https://doi.org/10.1073/pnas.1701563114>
- Mccarthy, G. D., Brown, P. J., Flagg, C. N., Goni, G., Houpert, L., Hughes, C. W., Hummels, R., Inall, M., Jochumsen, K., Larsen, K. M. H., Lherminier, P., Meinen, C. S., Moat, B. I., Rayner, D., Rhein, M., Roessler, A., Schmid, C., & Smeed, D. A. (2020). Sustainable Observations of the AMOC: Methodology and Technology. *Reviews of Geophysics*, 58(1). <https://doi.org/10.1029/2019rg000654>
- Mccarthy, G., Frajka-Williams, E., Johns, W. E., Baringer, M. O., Meinen, C. S., Bryden, H. L., Rayner, D., Duche, A., Roberts, C., & Cunningham, S. A. (2012). Observed interannual variability of the Atlantic meridional overturning circulation at 26.5°N. *Geophysical Research Letters*, 39(19), n/a-n/a. <https://doi.org/10.1029/2012gl052933>
- Menze, S., Ingvaldsen, R. B., Haugan, P., Fer, I., Sundfjord, A., Beszczynska-Moeller, A., &

- Falk-Petersen, S. (2019). Atlantic Water Pathways Along the North-Western Svalbard Shelf Mapped Using Vessel-Mounted Current Profilers. *Journal of Geophysical Research: Oceans*, 124(3), 1699–1716. <https://doi.org/10.1029/2018jc014299>
- Mesinger, F., & Arakawa, A. (1976). Numerical methods used in atmospheric models, GARP Publication Series, No. 14. In *Global Atmospheric Research Program, World Meteorological Organization, Geneva (Switzerland)*.
- Moore, G. W. K., Våge, K., Renfrew, I. A., & Pickart, R. S. (2022). Sea-ice retreat suggests re-organization of water mass transformation in the Nordic and Barents Seas. *Nature Communications*, 13(1). <https://doi.org/10.1038/s41467-021-27641-6>
- Morison, J., Kwok, R., Peralta-Ferriz, C., Alkire, M., Rigor, I., Andersen, R., & Steele, M. (2012). Changing Arctic Ocean freshwater pathways. *Nature*, 481(7379), 66–70. <https://doi.org/10.1038/nature10705>
- Muilwijk, M., Smedsrud, L. H., Ilicak, M., & Drange, H. (2018). Atlantic Water Heat Transport Variability in the 20th Century Arctic Ocean From a Global Ocean Model and Observations. *Journal of Geophysical Research: Oceans*, 123(11), 8159–8179. <https://doi.org/10.1029/2018JC014327>
- Myers, P. G., & Donnelly, C. (2008). Water mass transformation and formation in the Labrador Sea. *Journal of Climate*, 21(7), 1622–1638. <https://doi.org/10.1175/2007JCLI1722.1>
- Myers, P. G., Donnelly, C., & Ribergaard, M. H. (2009). *Structure and variability of the West Greenland Current in Summer derived from 6 repeat standard sections*. 80(1–2), 93–112. <https://doi.org/10.1016/j.pocean.2008.12.003>
- Onarheim, I. H., & Årthun, M. (2017). Toward an ice-free Barents Sea. *Geophysical Research Letters*, 44(16), 8387–8395. <https://doi.org/10.1002/2017GL074304>

- Orvik, K. A., Skagseth, Ø., & Mork, M. (2001). Atlantic inflow to the Nordic Seas: Current structure and volume fluxes from moored current meters, VM-ADCP and SeaSoar-CTD observations, 1995-1999. *Deep-Sea Research Part I: Oceanographic Research Papers*, 48(4), 937–957. [https://doi.org/10.1016/S0967-0637\(00\)00038-8](https://doi.org/10.1016/S0967-0637(00)00038-8)
- Oziel, L., Sirven, J., & Gascard, J. C. (2016). The Barents Sea frontal zones and water masses variability (1980-2011). *Ocean Science*, 12(1), 169–184. <https://doi.org/10.5194/os-12-169-2016>
- P. Raj, R., Chatterjee, S., Bertino, L., Turiel, A., & Portebella, M. (2019). The Arctic Front and its variability in the Norwegian Sea. In *Ocean Science Discussions*. Copernicus GmbH. <https://doi.org/10.5194/os-2018-159>
- Pérez-Hernández, M. D., Pickart, R. S., Torres, D. J., Bahr, F., Sundfjord, A., Ingvaldsen, R., Renner, A. H. H., Beszczynska-Möller, A., von Appen, W. J., & Pavlov, V. (2019). Structure, Transport, and Seasonality of the Atlantic Water Boundary Current North of Svalbard: Results From a Yearlong Mooring Array. *Journal of Geophysical Research: Oceans*, 124(3), 1679–1698. <https://doi.org/10.1029/2018JC014759>
- Petit, T., Lozier, M. S., Josey, S. A., & Cunningham, S. A. (2020). Atlantic Deep Water Formation Occurs Primarily in the Iceland Basin and Irminger Sea by Local Buoyancy Forcing. *Geophysical Research Letters*, 47(22). <https://doi.org/10.1029/2020gl091028>
- Pnyushkov, A. V., Polyakov, I. V., Ivanov, V. V., Aksenov, Y., Coward, A. C., Janout, M., & Rabe, B. (2015). Structure and variability of the boundary current in the Eurasian Basin of the Arctic Ocean. *Deep-Sea Research Part I: Oceanographic Research Papers*, 101(March), 80–97. <https://doi.org/10.1016/j.dsr.2015.03.001>
- Polyakov, I. V., Alkire, M. B., Bluhm, B. A., Brown, K. A., Carmack, E. C., Chierici, M.,

- Danielson, S. L., Ellingsen, I., Ershova, E. A., Gårdfeldt, K., Ingvaldsen, R. B., Pnyushkov, A. V., Slagstad, D., & Wassmann, P. (2020). Borealization of the Arctic Ocean in Response to Anomalous Advection From Sub-Arctic Seas. *Frontiers in Marine Science*, 7(July).
<https://doi.org/10.3389/fmars.2020.00491>
- Polyakov, I. V., Pnyushkov, A. V., Alkire, M. B., Ashik, I. M., Baumann, T. M., Carmack, E. C., Goszczko, I., Guthrie, J., Ivanov, V. V., Kanzow, T., Krishfield, R., Kwok, R., Sundfjord, A., Morison, J., Rember, R., & Yulin, A. (2017). Greater role for Atlantic inflows on sea-ice loss in the Eurasian Basin of the Arctic Ocean. *Science*, 356(6335), 285–291.
<https://doi.org/10.1126/science.aai8204>
- Polyakov, I. V., Rippeth, T. P., Fer, I., Baumann, T. M., Carmack, E. C., Ivanov, V. V., Janout, M., Padman, L., Pnyushkov, A. V., & Rember, R. (2020). Intensification of Near-Surface Currents and Shear in the Eastern Arctic Ocean. *Geophysical Research Letters*, 47(16).
<https://doi.org/10.1029/2020gl089469>
- Proshutinsky, A., Krishfield, R., Toole, J. M., Timmermans, M. -L., Williams, W., Zimmermann, S., Yamamoto-Kawai, M., Armitage, T. W. K., Dukhovskoy, D., Golubeva, E., Manucharyan, G. E., Platov, G., Watanabe, E., Kikuchi, T., Nishino, S., Itoh, M., Kang, S. -H., Cho, K. -H., Tateyama, K., & Zhao, J. (2019). Analysis of the Beaufort Gyre Freshwater Content in 2003–2018. *Journal of Geophysical Research: Oceans*, 124(12), 9658–9689.
<https://doi.org/10.1029/2019jc015281>
- Rhein, M., Steinfeldt, R., Kieke, D., Stendardo, I., & Yashayaev, I. (2017). Ventilation variability of Labrador Sea Water and its impact on oxygen and anthropogenic carbon: A review. In *Philosophical Transactions of the Royal Society A: Mathematical, Physical and Engineering Sciences* (Vol. 375, Issue 2102). Royal Society Publishing.

<https://doi.org/10.1098/rsta.2016.0321>

- Rudels, B., Korhonen, M., Schauer, U., Pisarev, S., Rabe, B., & Wisotzki, A. (2015). Circulation and transformation of Atlantic water in the Eurasian Basin and the contribution of the Fram Strait inflow branch to the Arctic Ocean heat budget. *Progress in Oceanography*, *132*, 128–152. <https://doi.org/10.1016/j.pocean.2014.04.003>
- Schlichtholz, P. (2011). Influence of oceanic heat variability on sea ice anomalies in the Nordic Seas. *Geophysical Research Letters*, *38*(5), n/a-n/a. <https://doi.org/10.1029/2010gl045894>
- Schulz, K., Janout, M., Lenn, Y., Ruiz-Castillo, E., Polyakov, I., Mohrholz, V., Tippenhauer, S., Reeve, K. A., Hölemann, J., Rabe, B., & Vredenburg, M. (2021). On the Along-Slope Heat Loss of the Boundary Current in the Eastern Arctic Ocean. *Journal of Geophysical Research: Oceans*, *126*(2). <https://doi.org/10.1029/2020jc016375>
- Skagseth, Ø., Furevik, T., Ingvaldsen, R., Loeng, H., Mork, K. A., Orvik, K. A., & Ozhigin, V. (2008). Volume and Heat Transports to the Arctic Ocean Via the Norwegian and Barents Seas. In *Arctic–Subarctic Ocean Fluxes* (pp. 45–64). Springer Netherlands. https://doi.org/10.1007/978-1-4020-6774-7_3
- Smedsrud, L H, Ingvaldsen, R., Nilsen, J. E. Ø., & Skagseth, Ø. (2010). *Heat in the Barents Sea: transport, storage, and surface fluxes*. *6*(1), 219–234. <https://doi.org/10.5194/os-6-219-2010>
- Smedsrud, Lars H., Esau, I., Ingvaldsen, R. B., Eldevik, T., Haugan, P. M., Li, C., Lien, V. S., Olsen, A., Omar, A. M., Risebrobakken, B., Sandø, A. B., Semenov, V. A., & Sorokina, S. A. (2013). The role of the Barents Sea in the Arctic climate system. *Reviews of Geophysics*, *51*(3), 415–449. <https://doi.org/10.1002/rog.20017>
- Smith, G. C., Roy, F., Mann, P., Dupont, F., Brasnett, B., Lemieux, J.-F., Laroche, S., & Bélair, S. (2014). A new atmospheric dataset for forcing ice-ocean models: Evaluation of

- re-forecasts using the Canadian global deterministic prediction system. *Quarterly Journal of the Royal Meteorological Society*, 140(680), 881–894. <https://doi.org/10.1002/qj.2194>
- Speer, K., & Tziperman, E. (1992a). Rates of Water Mass Formation in the North Atlantic Ocean. In *Journal of Physical Oceanography* (Vol. 22, Issue 1, pp. 93–104). [https://doi.org/10.1175/1520-0485\(1992\)022<0093:rowmfi>2.0.co;2](https://doi.org/10.1175/1520-0485(1992)022<0093:rowmfi>2.0.co;2)
- Speer, K., & Tziperman, E. (1992b). Rates of Water Mass Formation in the North Atlantic Ocean. *Journal of Physical Oceanography*, 22(1), 93–104. [https://doi.org/10.1175/1520-0485\(1992\)022<0093:rowmfi>2.0.co;2](https://doi.org/10.1175/1520-0485(1992)022<0093:rowmfi>2.0.co;2)
- Spielhagen, R. F., Werner, K., Sørensen, S. A., Zamelczyk, K., Kandiano, E., Budeus, G., Husum, K., Marchitto, T. M., & Hald, M. (2011). Enhanced modern heat transfer to the arctic by warm atlantic water. *Science*, 331(6016), 450–453. <https://doi.org/10.1126/science.1197397>
- Spren, G., Steur, L., Divine, D., Geland, S., Hansen, E., & Kwok, R. (2020). Arctic Sea Ice Volume Export Through Fram Strait From 1992 to 2014. *Journal of Geophysical Research: Oceans*, 125(6). <https://doi.org/10.1029/2019jc016039>
- Stadnyk, T. A., Tefs, A., Broesky, M., Déry, S. J., Myers, P. G., Ridenour, N. A., Koenig, K., Vonderbank, L., & Gustafsson, D. (2021). Changing freshwater contributions to the Arctic. *Elementa: Science of the Anthropocene*, 9(1). <https://doi.org/10.1525/elementa.2020.00098>
- Straneo, F. (2006). Heat and freshwater transport through the central Labrador Sea. *Journal of Physical Oceanography*, 36(4), 606–628. <https://doi.org/10.1175/JPO2875.1>
- Stroeve, J., Holland, M. M., Meier, W., Scambos, T., & Serreze, M. (2007). Arctic sea ice decline: Faster than forecast. *Geophysical Research Letters*, 34(9), n/a-n/a. <https://doi.org/10.1029/2007gl029703>

- Tesdal, J., & Haine, T. W. N. (2020). Dominant Terms in the Freshwater and Heat Budgets of the Subpolar North Atlantic Ocean and Nordic Seas From 1992 to 2015. *Journal of Geophysical Research: Oceans*, *125*(10). <https://doi.org/10.1029/2020jc016435>
- Timmermans, M., & Marshall, J. (2020). Understanding Arctic Ocean Circulation: A Review of Ocean Dynamics in a Changing Climate. *Journal of Geophysical Research: Oceans*, *125*(4). <https://doi.org/10.1029/2018jc014378>
- Wang, Q., Wang, X., Wekerle, C., Danilov, S., Jung, T., Koldunov, N., Lind, S., Sein, D., Shu, Q., & Sidorenko, D. (2019). Ocean Heat Transport Into the Barents Sea: Distinct Controls on the Upward Trend and Interannual Variability. *Geophysical Research Letters*, *46*(22), 13180–13190. <https://doi.org/10.1029/2019GL083837>
- Wang, Q., Wekerle, C., Wang, X., & Danilov, S. (2020). *Intensification of the Atlantic Water Supply to the Arctic Ocean Through Fram Strait Induced by Arctic Sea Ice Decline*. <https://doi.org/10.1029/2019GL086682>
- Wekerle, C., Hattermann, T., Wang, Q., Crews, L., Von Appen, W.-J., & Danilov, S. (2020). Properties and dynamics of mesoscale eddies in Fram Strait from a comparison between two high-resolution ocean–sea ice models. *Ocean Science*, *16*(5), 1225–1246. <https://doi.org/10.5194/os-16-1225-2020>
- Woodgate, R. (2013). Arctic Ocean Circulation – going around at the top of the world. *Nature Ed. Knowledge, February 2012*, 1–15.
- Yashayaev, I., & Loder, J. W. (2016). Recurrent replenishment of Labrador Sea Water and associated decadal-scale variability. *Journal of Geophysical Research: Oceans*, *121*(11), 8095–8114. <https://doi.org/10.1002/2016jc012046>
- Zhurbas, N., & Kuzmina, N. (2020). Variability of the thermohaline structure and transport of

Atlantic water in the Arctic Ocean based on NABOS (Nansen and Amundsen Basins Observing System) hydrography data. *Ocean Science*, 16(2), 405–421.

<https://doi.org/10.5194/os-16-405-2020>